Direct numerical simulation of hypersonic turbulent boundary layers. Part 4. Effect of high enthalpy

L. Duan and M. P. Martín

Journal of Fluid Mechanics / Volume 684 / October 2011, pp 25 - 59
DOI: 10.1017/jfm.2011.252, Published online: 06 September 2011

J. Fluid Mech. (2011), *vol.* 684, *pp.* 25–59.
doi:10.1017/jfm.2011.252

Direct numerical simulation of hypersonic turbulent boundary layers. Part 4. Effect of high enthalpy

L. Duan and M. P. Martín†

Department of Aerospace Engineering, University of Maryland, College Park, MD 20742, USA

(Received 20 October 2010; revised 17 February 2011; accepted 1 June 2011;
first published online 6 September 2011)

In this paper we present direct numerical simulations (DNS) of hypersonic turbulent boundary layers to study high-enthalpy effects. We study high- and low-enthalpy conditions, which are representative of those in hypersonic flight and ground-based facilities, respectively. We find that high-enthalpy boundary layers closely resemble those at low enthalpy. Many of the scaling relations for low-enthalpy flows, such as van-Driest transformation for the mean velocity, Morkovin's scaling and the modified strong Reynolds analogy hold or can be generalized for high-enthalpy flows by removing the calorically perfect-gas assumption. We propose a generalized form of the modified Crocco relation, which relates the mean temperature and mean velocity across a wide range of conditions, including non-adiabatic cold walls and real gas effects. The DNS data predict Reynolds analogy factors in the range of those found in experimental data at low-enthalpy conditions. The gradient transport model approximately holds with turbulent Prandtl number and turbulent Schmidt number of order unity. Direct compressibility effects remain small and insignificant for all enthalpy cases. High-enthalpy effects have no sizable influence on turbulent kinetic energy (TKE) budgets or on the turbulence structure.

Key words: compressible turbulence, turbulent boundary layers, turbulent reacting flows

1. Introduction

Strong bow and leading-edge shock waves, and large kinetic energy dissipation on hypersonic vehicles make boundary layers extremely hot. The high-enthalpy condition in such flows leads to real-gas effects (RGE), which include internal (vibrational and electronic) excitation, dissociation of air molecules, hence variable heat capacities and thermal and chemical non-equilibrium. As a result, significant deviation from the perfect-gas approximation occurs at such flow conditions.

For hypersonic turbulent boundary layers at high enthalpy, experimental measurements are extremely challenging. There are very few flight tests described in the open literature, and these tests generally provide limited turbulence data with large uncertainties. Although there are ground-based wind tunnel tests that provide data with acceptable experimental uncertainties, most hypersonic ground tests for turbulence cannot match the high total enthalpy levels typical of hypersonic flight. For these reasons, the validation of turbulence models with wind tunnel data involves significant extrapolation to flight enthalpies (Roy & Blottner 2006), and many

† Email address for correspondence: pmartin@umiacs.umd.edu

important parameters, such as turbulent Prandtl number and turbulent Schmidt number, are specified as empirical constants without much justification (Wright, White & Mangini 2009).

Direct numerical simulations (DNS) provide a vast amount of accurate data that can be used to study hypersonic turbulent boundary layers. Most previous DNS studies have been carried out at low-enthalpy, non-reacting conditions. For example, DNS of non-reacting turbulent boundary layers have been performed by Guarini *et al.* (2000) at Mach 2.5, Pirozzoli, Grasso & Gatski (2004) at Mach 2.25, Maeder, Adams & Kleiser (2001) at Mach 3, 4.5 and 6, Duan, Beekman & Martín (2010) at Mach 5 with wall-to-free-stream temperature ratio varying from 1.0 to 5.4, Duan, Beekman & Martín (2011) with free-stream Mach number varying from 0.3 to 12.0, and Dong & Zhou (2010) with Mach number varying from 2.5 to 6.0. There are only a few DNS of turbulent boundary layers under high-enthalpy conditions. Martín & Candler (1998, 1999), Martín (2000), Martín & Candler (2001), Martín (2003) and Duan & Martín (2009*a*,*b*) use simplified single dissociation/recombination reaction mechanisms and constant species heat capacities to study the nonlinear interaction between turbulence and finite-rate chemical reactions in the presence of predominantly exothermic or endothermic reactions in isotropic turbulence and turbulent boundary layers. Duan & Martín (2010) study and assess the presence and effects of turbulence–chemistry interaction for hypersonic conditions in the Earth's atmosphere. An assessment of turbulence and mean flow scalings, as well as of the influence of high enthalpy on turbulence statistics and coherent structures has not yet been performed.

One of the most important scaling laws for compressible turbulent boundary layers is Morkovin's hypothesis, or the weakly compressibility hypothesis (Morkovin 1962), which argues that for moderate free-stream Mach numbers, the differences from incompressible turbulence can be accounted for by mean variations of fluid properties. This is the basis for the van Driest transformation, a velocity scaling that accounts for the fluid-property variations to collapse compressible flow data onto the 'universal' incompressible distribution. Another important factor in compressible turbulent boundary layer analysis is the strong Reynolds analogy (SRA), which relates the temperature fluctuations to the streamwise velocity fluctuations and is used to extend incompressible turbulence models to compressible flows. Although the validity of Morkovin's hypothesis and the SRA has been assessed across a wide range of free-stream Mach numbers and wall temperatures under low-enthalpy conditions, equivalent information is not yet known for high-enthalpy environments. Furthermore, the character of the turbulence structure at high-enthalpy conditions has not yet been studied.

In this paper, we present a DNS study of turbulent boundary layer flow to investigate the influence of enthalpy conditions on turbulence statistics and coherent structures by comparing DNS results under low- and high-enthalpy conditions in air. The paper is structured as follows. Flow conditions and simulation details are given in § 2. Turbulence statistics are given in § 3. The relation between skin friction and heat transfer are discussed in § 4. A study of the strong Reynolds analogy is given in § 5. An assessment of the gradient transport assumption is provided in § 6. Turbulent kinetic energy budgets are given in § 7. Compressibility effects are investigated in § 8. Turbulence structure analyses are given in § 9. Finally, conclusions are drawn in § 10.

2. Simulation details

2.1. Governing equations, constitutive relations and numerical method

The equations describing the unsteady motion of a reacting fluid are given by the species mass, mass-averaged momentum, and total energy conservation equations, which, neglecting thermal non-equilibrium, are

$$\frac{\partial \rho_s}{\partial t} + \frac{\partial}{\partial x_j}(\rho_s u_j + J_{sj}) = w_s, \tag{2.1}$$

$$\frac{\partial \rho u_i}{\partial t} + \frac{\partial}{\partial x_j}(\rho u_i u_j + p\delta_{ij} - \sigma_{ij}) = 0, \tag{2.2}$$

$$\frac{\partial E}{\partial t} + \frac{\partial}{\partial x_j}\left((E+p)u_j - u_i\sigma_{ij} + q_j + \sum_s J_{sj}h_s\right) = 0, \tag{2.3}$$

where w_s represents the rate of production of species s due to chemical reactions; ρ_s is the density of species s; u_j is the mass-averaged velocity in the j direction; $\rho = \sum_s \rho_s$ is the total flow density; p is the pressure, which is given by

$$p = \sum_s \rho_s \frac{\hat{R}}{M_s} T, \tag{2.4}$$

where $\hat{R}$ is the universal gas constant, M_s is the molecular weight of species s and T is the translational temperature; σ_{ij} is the shear stress tensor, which is given by a linear stress–strain relationship

$$\sigma_{ij} = 2\mu S_{ij} - \tfrac{2}{3}\mu\delta_{ij}S_{kk}, \tag{2.5}$$

where $S_{ij} = (1/2)(\partial u_i/\partial x_j + \partial u_j/\partial x_i)$ is the strain rate tensor and μ is the mixture viscosity; h_s is the specific enthalpy of species s; q_j is the conductive heat flux described by Fourier's law $q_j = -\kappa(\partial T/\partial x_j)$ where κ is the mixture thermal conductivity. E is the total energy per unit volume given by

$$E = \sum_s \rho_s \left(h_s - \frac{\hat{R}}{M_s}T\right) + \frac{1}{2}\rho u_i u_i, \tag{2.6}$$

J_{sj} is the diffusive mass flux of species s given by Fick's law

$$J_{sj} = -\rho D \frac{\partial Y_s}{\partial x_j}, \tag{2.7}$$

where Y_s is the species mass fraction, $Y_s = \rho_s/\rho$, and D is the diffusion coefficient given in terms of the Lewis number

$$D = \frac{\kappa}{\rho C_p Le}, \tag{2.8}$$

with $C_p = \sum_s Y_s C_{ps}$.

The thermodynamic properties of high-temperature air species, including species enthalpy h_s and species heat capacity C_{ps} are computed by NASA Lewis curve fits (Gordon & McBride 1994). Mixture transport properties μ and κ are calculated using the Gupta (Gupta *et al.* 1990)–Yos (Yos 1963) mixing rule. Unity Lewis number is used for calculating species diffusion flux J_{sj}.

The reactions for air are modelled using the air-five-species mechanism: N_2, O_2, NO, N, and O with Arrhenius parameters (Park 1990), shown as follows:

$$N_2 + M \rightleftharpoons 2N + M, \tag{2.9}$$

$$O_2 + M \rightleftharpoons 2O + M, \tag{2.10}$$

$$NO + M \rightleftharpoons N + O + M, \tag{2.11}$$

$$N_2 + O \rightleftharpoons NO + N, \tag{2.12}$$

$$NO + O \rightleftharpoons O_2 + N. \tag{2.13}$$

This mechanism represents realistic reactions of air in the absence of ionization and is a good approximation at temperatures less than about 10 000 K.

For low-enthalpy flow simulations, calorically perfect air with constant heat capacities is assumed. The viscosity μ is computed using a power law with the form

$$\mu = \mu_\delta \left(\frac{T}{T_\delta} \right)^{0.76}, \tag{2.14}$$

with T_δ and μ_δ being the boundary layer edge temperature and viscosity, respectively; μ_δ is computed using the Sutherland law for $T_\delta \geqslant 170$ K and Keyes model (Keyes 1951) for $T_\delta < 170$ K. The details of the perfect gas air model and its molecular transport properties are given in Roy & Blottner (2006).

For numerical discretization, we use a linearly and nonlinearly optimized, 4th-order-accurate weighted essentially-non-oscillatory (WENO) method (Martín *et al.* 2006; Taylor & Martín 2007) for the convective terms, a 4th-order-accurate central difference scheme for the viscous terms and a 3rd-order-accurate low-storage Runge–Kutta method (Williamson 1980) for time integration. The WENO scheme has shock-capturing capability to ensure numerical stability while at the same time has optimal bandwidth efficiency and minimum numerical dissipation. Details of code validation, including the comparison with existing experimental data and a well-established numerical solver for high-enthalpy flows (Wright *et al.* 2009), have been given in Martín (2007) and Duan & Martín (2009*c*).

2.2. *Flow conditions*

For high-enthalpy cases, we consider the boundary layer flow over a flat plate flying at an angle of attack, at Mach 21 and at an altitude of 30 km. Angles of attack of $\alpha = 35^\circ$ and 8°, are considered, denoted as Wedge35 and Wedge8, respectively. For case Wedge35, the large angle of attack results in high post-shock temperature and chemically dissociated gas in the boundary layer edge, and the boundary layer is representative of that on a blunt body. For case Wedge8, the angle of attack is small and the flow at the boundary layer edge remains cold and non-reacting although, due to recovery effects, the temperature rises within the boundary layer and the flow is partially dissociated. Thus, the boundary layer in this case is typical of that on a slender-body hypersonic vehicle. Both cases have an enthalpy level of 20 MJ kg^{-1}.

In addition, in order to investigate the influence of species boundary conditions on the turbulent flow field, we consider 'supercatalytic' and 'non-catalytic' surface models for each flow condition. These surface models represent limiting conditions that might occur. The non-catalytic wall assumes no atom recombination and minimal enthalpy recovery at the surface, and it is given by

$$\left(\frac{\partial Y}{\partial n} \right)_{s,w} = 0, \tag{2.15}$$

with n being the unit vector in the wall normal direction. In contrast, the supercatalytic wall assumes infinitely fast atom recombination and maximum enthalpy recovery at the

Case	M_∞	ρ_∞ (kg m^{-3})	T_∞ (K)	T_w (K)	$h_{t,\infty}$ (MJ kg^{-1})	α (deg.)
Wedge	21	0.0184	226.5	2400.0	20	8 and 35
LowH_M3	3.5	0.0184	226.5	125.0	0.78	0
LowH_M10	10.5	0.00016	34.0	86.0	0.79	0

TABLE 1. Free-stream and wall parameters for the larger domain finite-volume RANS calculations.

surface. In this case, the chemical composition at the wall recovers to that in the free stream and the species boundary condition

$$Y_{s,w} = Y_{s,\infty}, \tag{2.16}$$

where $Y_{s,\infty}$ is the flow composition for the cold air upstream of the leading-edge shock and may be different from the post-shock boundary layer edge composition $Y_{s,\delta}$. For simplicity, we refer to Wedge35 with supercatalytic and non-catalytic wall as Wedge35supercata and Wedge35noncata, respectively. Similar definitions are used for case Wedge8.

For low-enthalpy cases, we consider a flat plate at zero angle of attack to the free stream, with the boundary layer edge Mach number and the ratio of wall to adiabatic temperature approximately matching those for case Wedge35 and Wedge8, and the corresponding cases are LowH_M3 and LowH_M10, respectively. In this way, we define the low-enthalpy flow counterparts of cases Wedge35 and Wedge8 to provide a baseline for comparison with the high-enthalpy cases. Both low-enthalpy conditions have an enthalpy level of approximately 0.8 MJ kg^{-1}, which is typical of most ground-based hypersonic facilities, although the flow conditions themselves might not be realistic. Perfect gas is assumed for the low-enthalpy cases.

Table 1 provides Mach number, density, temperature, and total enthalpy, M_∞, ρ_∞, T_∞ and $h_{t,\infty}$, respectively, for the cold air upstream of the leading-edge shock as well as the inclination angle relative to the free stream for high- and low-enthalpy cases. We have used subscripts ∞ to denote the free-stream quantities upstream of the leading-edge shock and T_w is the wall temperature.

The initial DNS flow field is obtained by first extracting the mean profiles from the Reynolds-averaged Navier–Stokes (RANS) calculation and then superimposing a fluctuating field. The mean flow conditions are extracted from larger domain finite-volume RANS calculations using data parallel line relaxation (DPLR) (Wright *et al.* 2009), solving the equations described in § 2.1. Figure 1 shows the computational domain for the RANS solution and a sketch of the DNS subdomain for cases Wedge35 and Wedge8. The location of the DNS subdomain is significantly downstream of the leading edge, where the Reynolds number is large enough for the flow to be fully turbulent. In this region, the effect of thermal non-equilibrium is expected to be unimportant. In addition, the large distance between the leading edge of the wedge and the location of the DNS subdomain allows enough relaxation time for chemical reactions to progress, as indicated by figure 2, which plots the Damköhler number $Da_s = (L/u_\infty)/(\rho_s/w_s)$ at the location of the DNS subdomain. The Damköhler number is defined as the ratio of flow residence time to chemical relaxation time, with L the distance between the leading edge of the wedge and the location of the DNS subdomain. It is shown that the flow residence time at the selected DNS location is comparable with the characteristic chemical relaxation time for most species. For the

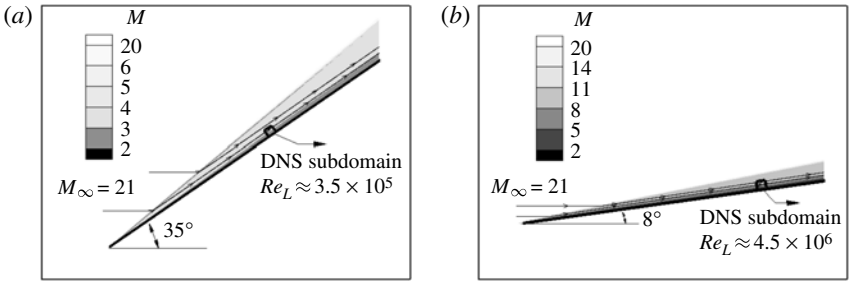

FIGURE 1. DNS subdomain from RANS solution for the study of high-enthalpy effects on turbulence. The Reynolds number $Re_L = \rho_\infty u_\infty L/\mu_\infty$, where L is the distance between the leading edge of the lifting body and the location of the DNS subdomain. (*a*) Wedge35; (*b*) Wedge8.

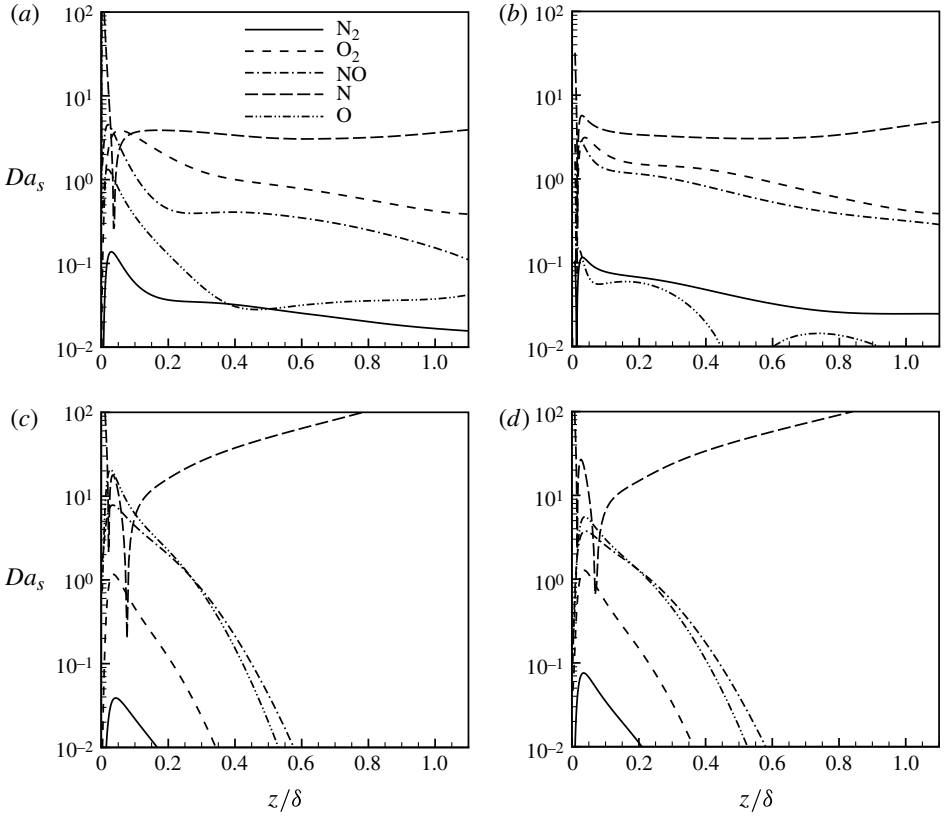

FIGURE 2. Damköhler number $Da_s \equiv (L/u_\infty)/(\rho_s/w_s)$ from RANS solution at the location of the DNS subdomain. L is the distance between the leading edge of the wedge and the location of the DNS subdomain. (*a*) Wedge35supercata; (*b*) Wedge35noncata; (*c*) Wedge8supercata; (*d*) Wedge8noncata.

low-enthalpy cases, however, the location of the DNS subdomain has been chosen to approximately match the Reynolds number with the corresponding high-enthalpy case, as shown in table 2.

Case	M_δ	ρ_δ (kg m^{-3})	T_δ (K)	T_w (K)	T_w/T_{aw}	Re_θ	Re_τ	$Re_{\delta 2}$	θ (mm)	H	δ (mm)
Wedge35supercata	3.4	0.173000	4474.5	2400.0	0.13	966.2	906.4	1544.5	0.154	1.79	1.397
Wedge35noncata	3.4	0.172000	4505.9	2400.0	0.13	1011.1	910.3	1553.9	0.162	2.18	1.611
Wedge8supercata	9.4	0.070000	1290.9	2400.0	0.13	3026.1	786.0	1952.0	0.363	15.00	9.090
Wedge8noncata	9.3	0.072000	1234.5	2400.0	0.13	3058.1	741.0	1941.0	0.360	14.90	8.870
LowH_M3	3.4	0.018400	234.2	125.0	0.17	958.1	937.9	1554.5	0.767	2.84	8.464
LowH_M10	9.0	0.000174	47.9	86.0	0.12	2451.6	905.9	1651.7	42.000	18.40	1308.100

TABLE 2. Dimensional bounday layer edge and wall parameters for the DNS cases. $T_{aw} = T_\infty(1 + r((\gamma - 1)/2)M_\infty^2)$ with $r = 0.9$.

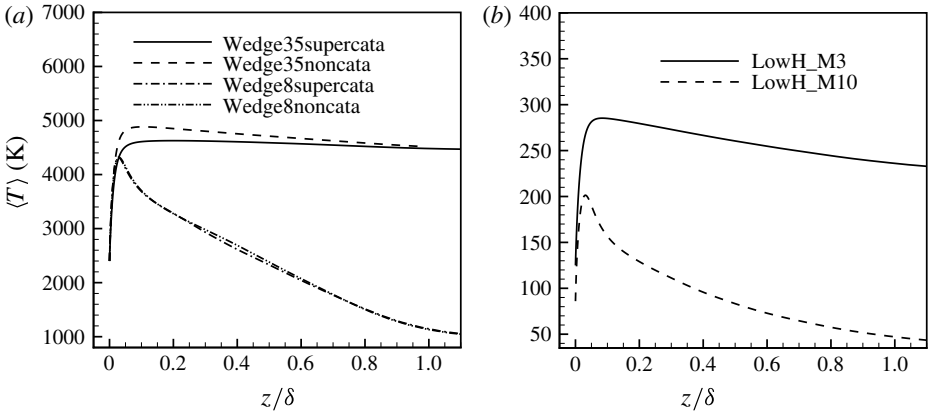

FIGURE 3. Mean flow temperature across the boundary layer for various DNS cases.

The fluctuating field is obtained by transforming that of an incompressible turbulent boundary layer DNS using incompressible/compressible scaling laws. The details of this initialization technique are introduced by Martín (2007). The initial data are an educated guess for the DNS, which evolves to an exact solution after a short transient. On the wall boundary, non-slip conditions are used for the three velocity components. The wall temperature is prescribed and kept isothermal. Species boundary conditions for high-enthalpy cases are either supercatalytic or non-catalytic. The flow conditions on the top boundary are fixed edge conditions which are extracted from the RANS calculation. Periodic boundary conditions have been used in the streamwise and spanwise directions.

Table 2 lists the boundary layer edge conditions and wall parameters for all DNS cases after the initial transient, providing the boundary layer edge Mach number, density, and temperature, M_δ, ρ_δ, and T_δ, respectively, and boundary layer properties: momentum thickness, θ, shape factor, $H = \delta^*/\theta$ with δ^* the displacement thickness, boundary layer thickness δ, and different definitions of Reynolds number, with $Re_\theta \equiv \rho_\delta u_\delta \theta/\mu_\delta$, $Re_\tau \equiv \rho_w u_\tau \delta/\mu_w$, and $Re_{\delta 2} \equiv \rho_\delta u_\delta \theta/\mu_w$. We have used subscripts δ and w to denote quantities at the boundary layer edge and at the wall, respectively. u_τ is the friction velocity defined as $u_\tau = \sqrt{\tau_w/\rho_w}$ with τ_w being the wall shear stress. We keep Re_τ and $Re_{\delta 2}$ nearly constant, with Re_θ having an insignificant variation of approximately threefold across the cases.

At the selected high-enthalpy conditions, the maximum flow temperatures are above 4000 K (figure 3*a*), and significant real-gas effects exist. Figure 4(*a*) shows that the specific heat ratio $\gamma = C_p/C_v$ deviates significantly from the perfect-gas value of 1.4 throughout the boundary layer, and figure 4(*b*) shows that the flow is partially dissociated. For both low-enthalpy cases, the maximum flow temperatures are close to room temperature, as shown in figure 3(*b*), and any high-enthalpy real-gas effects are negligible.

2.3. *Numerical simulation parameters*

The computational domain is chosen to be large enough to contain a good sample of the large scales, while the grid resolution is fine enough to resolve the near wall structures (Martín 2007). The domain size ($L_x \times L_y \times L_z$), the grid size ($\Delta x \times \Delta y \times \Delta z$) and the number of grid points ($N_x \times N_y \times N_z$) are given in table 3. We take the streamwise, spanwise, and wall-normal directions to be x, y and z. We use

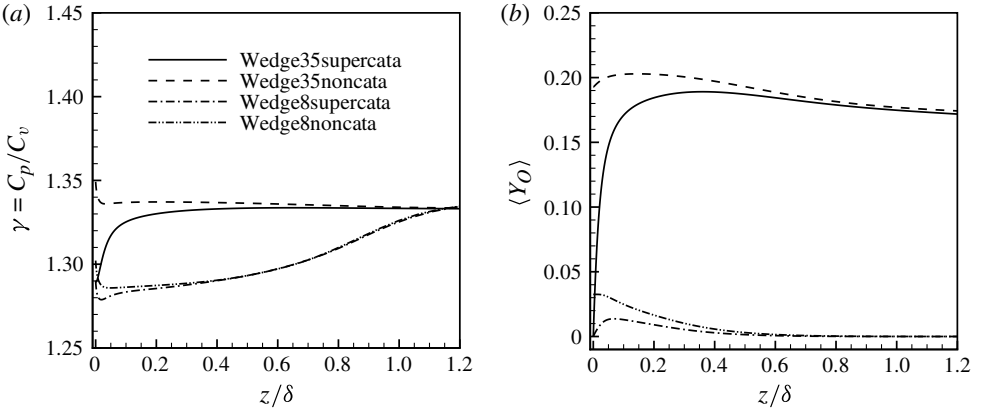

FIGURE 4. (*a*) Specific heat ratio $\gamma = C_p/C_v$ and (*b*) mass fraction of atomic oxygen $\overline{Y}_O$ for high-enthalpy DNS cases.

Case	L_x/δ	L_y/δ	L_z/δ	Δx^+	Δy^+	z_2^+	α	N_x	N_y	N_z
Wedge35supercata	17.2	1.7	4.3	26.6	4.0	0.19	1.068	576	384	110
Wedge35noncata	14.7	1.5	3.6	23.2	3.5	0.17	1.068	576	384	110
Wedge8supercata	19.5	2.8	5.6	26.7	5.7	0.26	1.067	576	384	110
Wedge8noncata	20.0	2.9	5.7	25.7	5.5	0.25	1.067	576	384	110
LowH_M3	16.6	2.1	4.0	27.1	5.1	0.17	1.063	576	384	120
LowH_M10	20.2	2.2	4.0	33.1	5.4	0.17	1.063	576	384	120

TABLE 3. Grid resolution and domain size for the DNS data.

uniform grids in the streamwise and spanwise directions as Δx^+ and Δy^+, where the superscript + indicates scaling with inner, or wall values, and geometrically stretched grids in the wall-normal direction, with $z_k = z_2(\alpha^{k-1} - 1)/(\alpha - 1)$, where k is the grid number in the wall-normal direction.

To assess the adequacy of the domain size, two-point correlations for the streamwise, spanwise and wall-normal velocity components are plotted in figure 5 at $z^+ = 15$ and $z/\delta = 0.1$ for case Wedge35supercata. The two-point correlations drop to zero for large separations, indicating that the computational domain is large enough to contain a good sample of the large scales. Similar results can be shown for other cases. To assess convergence, figure 6(*a–d*) plots the mean streamwise velocity, mean temperature, r.m.s. streamwise velocity and r.m.s. temperature for case Wedge35supercata with different grid sizes. All curves collapse to within 2 %, indicating that the grid is fine enough to converge the results. Similar convergence can be shown for skin friction and heat transfer. Grid convergence has been checked for all the other cases.

3. Flow statistics

Statistical averages are computed over streamwise and spanwise directions of each field; then an ensemble average is calculated over fields spanning around one non-dimensional time unit. The time is non-dimensionalized by δ/u_τ, which corresponds to around 20 large-eddy turnover times. During the sampling period, the variations

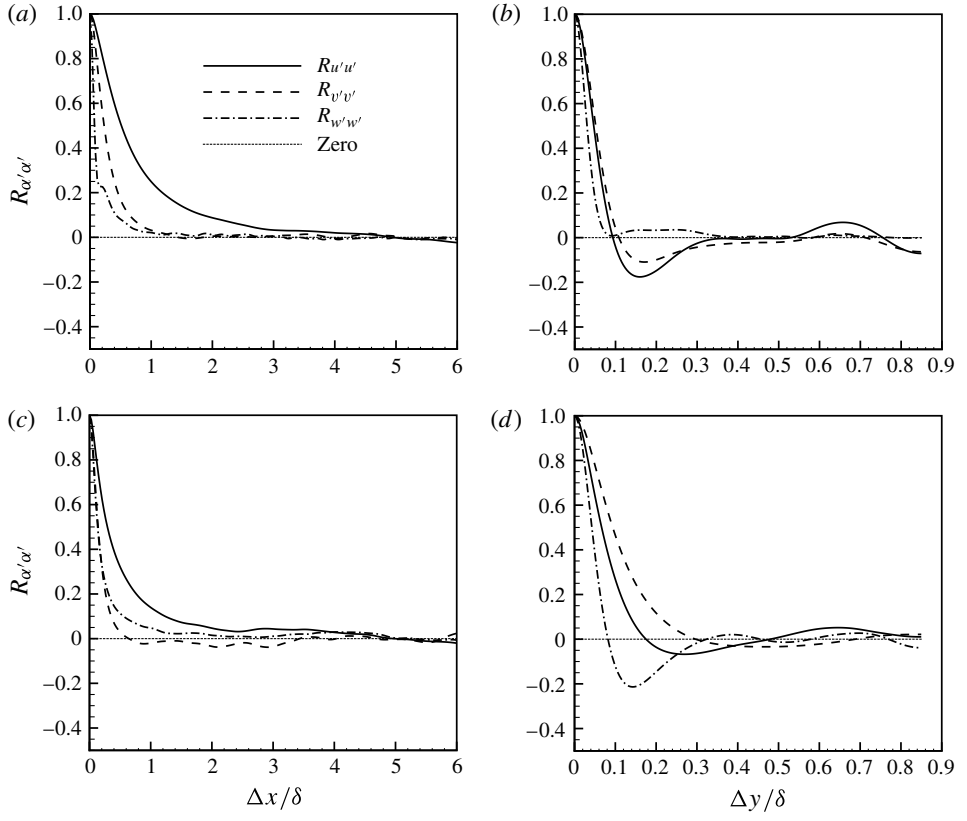

FIGURE 5. Two-point correlations $R_{\alpha'\alpha'}$ for streamwise, spanwise and wall-normal velocity components. Plotted versus (*a*) $\Delta x/\delta$ at $z^+ = 15$; (*b*) $\Delta y/\delta$ at $z^+ = 15$; (*c*) $\Delta x/\delta$ at $z/\delta = 0.1$; (*d*) $\Delta y/\delta$ at $z/\delta = 0.1$. Straight dash-dotted line represents the zero value.

in (δ^*, u_τ, C_f) are less than 5 % during the simulations, and periodic boundary conditions in the streamwise directions are justified (see Xu & Martín 2004). Both Reynolds and Favre averaging are used. The Reynolds average of f over the x and y directions will be denoted by $\bar{f}$, or $\langle f \rangle$, and fluctuations about this mean will be denoted by f'. The Favre average over the x and y directions, $\tilde{f}$, is a density-weighted average:

$$\tilde{f} = \frac{\overline{\rho f}}{\overline{\rho}}. \tag{3.1}$$

Fluctuations about the Favre average will be denoted by f''.

3.1. *Mean flow*

Figure 7 plots the van Driest transformed velocity, $\bar{U}_{VD}$. The data are insensitive to enthalpy conditions, and the log-region can be well described by $(1/\kappa)\log z^+ + C$ with $\kappa = 0.41$ and $C = 6.2$. Bradshaw (1977) suggests $\kappa = 0.41$ and $C = 5.2$ for turbulent boundary layers with zero pressure gradient over an adiabatic wall. The relatively larger value of C has also been observed for cold-wall hypersonic boundary layers by Maeder (2000) and Duan *et al.* (2010).

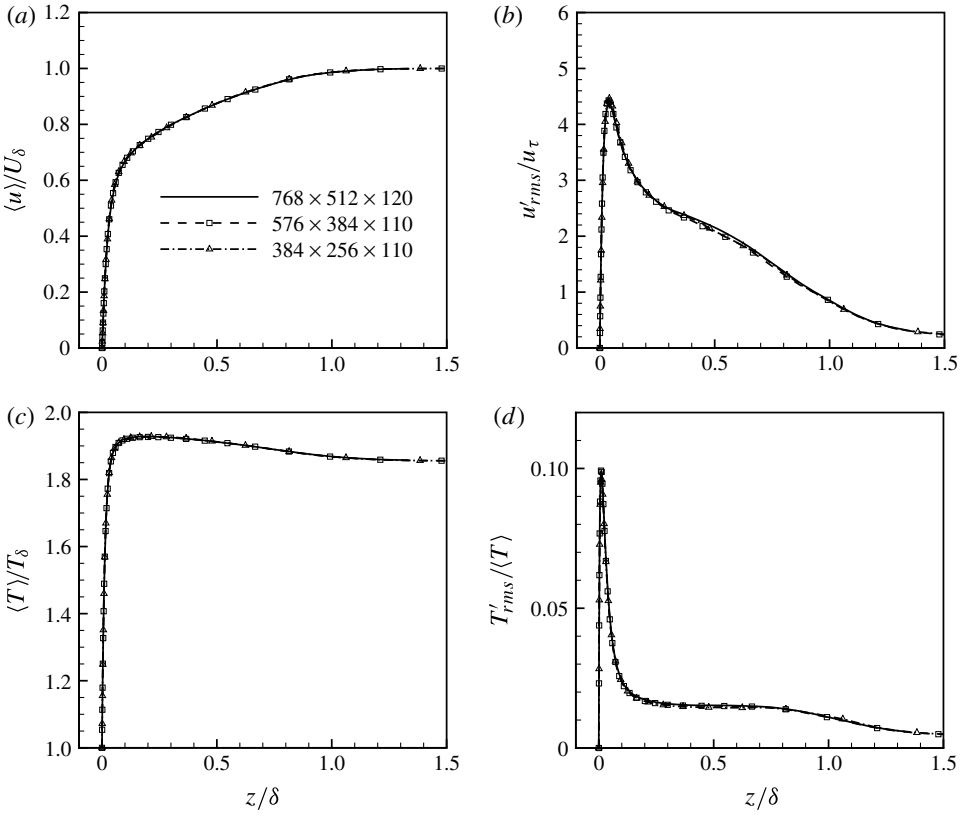

FIGURE 6. Convergence study for Wedge35supercata varying grid size, $N_x \times N_y \times N_z$.

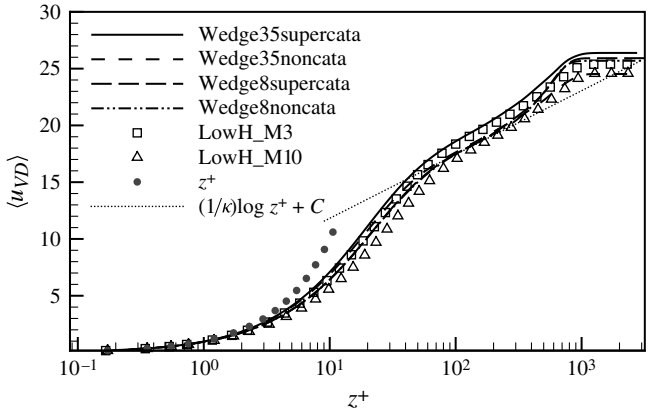

FIGURE 7. Van Driest transformed velocity for high- and low-enthalpy cases.

The modified Crocco relation by Walz (1969) is commonly used to relate the mean temperature and velocity in zero-pressure-gradient boundary layers, namely:

$$\frac{\tilde{T}}{T_\delta} = \frac{T_w}{T_\delta} + \frac{T_{aw} - T_w}{T_\delta}\left(\frac{\tilde{u}}{u_\delta}\right) + \frac{T_\delta - T_{aw}}{T_\delta}\left(\frac{\tilde{u}}{u_\delta}\right)^2, \tag{3.2}$$

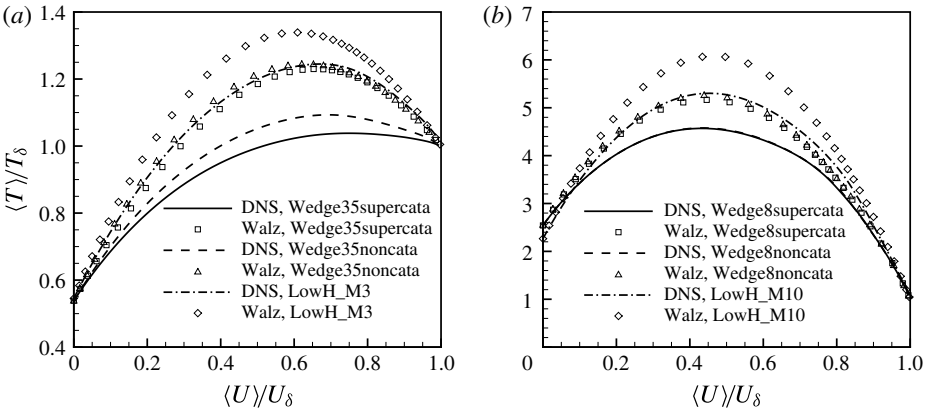

FIGURE 8. Walz's equation as expressed by (3.2) for high- and low-enthalpy cases. Lines: DNS; symbols: Walz's relation given by (3.2).

with $T_{aw} = T_\delta(1 + r((\gamma - 1)/2)M_\delta^2)$ and r the recovery factor assumed to be 0.9. Figure 8 plots this equation and the exact ratios for the DNS data. The temperature–velocity relation significantly deviates from (3.2), similar to the observation by Duan *et al.* (2010) for Mach 5 boundary layers on cold walls. Both the enthalpy condition and surface catalysis influence the temperature–velocity relation.

To remove the explicit dependence of the temperature–velocity relation on thermal and chemical models, we introduce the non-dimensional 'recovery enthalpy', which is defined as

$$h_r^* = \frac{\tilde{h}_r - h_w}{h_{aw} - h_w}, \tag{3.3}$$

with $\tilde{h}_r = \tilde{h} + r(\tilde{u}^2/2)$ and r the recovery factor, again assumed to be 0.9. At the wall $\tilde{h}_r = h_w$ and $h_r^* = 0$, while at $z = \delta$, $\tilde{h}_r = h_\delta + r(\tilde{u}_\delta^2/2) = h_{aw}$ and $h_r^* = 1$. Figure 9 plots the non-dimensional 'recovery enthalpy' h_r^* versus $\tilde{u}/u_\delta$. The data collapse across the flow conditions, indicating that $h_r^* = (\tilde{h}_r - h_w)/(h_{aw} - h_w) = f(\tilde{u}/u_\delta)$, or

$$\frac{\tilde{h}}{h_\delta} = \frac{h_w}{h_\delta} + \frac{h_{aw} - h_w}{h_\delta} f\left(\frac{\tilde{u}}{u_\delta}\right) - r\frac{\frac{1}{2}u_\delta^2}{h_\delta}\left(\frac{\tilde{u}}{u_\delta}\right)^2, \tag{3.4}$$

with $f(\tilde{u}/u_\delta)$ nearly independent of free-stream Mach number, wall temperature, surface catalysis and enthalpy conditions. In addition, figure 9 shows that $f(\tilde{u}/u_\delta)$ is close to $\tilde{u}/u_\delta$, but not exactly the same. The fitting of the DNS data gives

$$f\left(\frac{\tilde{u}}{u_\delta}\right) = 0.1741\left(\frac{\tilde{u}}{u_\delta}\right)^2 + 0.8259\left(\frac{\tilde{u}}{u_\delta}\right). \tag{3.5}$$

Equation (3.4) indicates that $\tilde{h} = h(\tilde{u})$, a relation which has been assumed by van Driest (1956) and Walz (1969) for deriving (3.2).

In general, the explicit functional form of the temperature–velocity relation depends on $\tilde{h} = h(\tilde{T}, \tilde{Y})$. When calorically perfect gas is assumed, i.e. $h = C_pT$, (3.4) can be

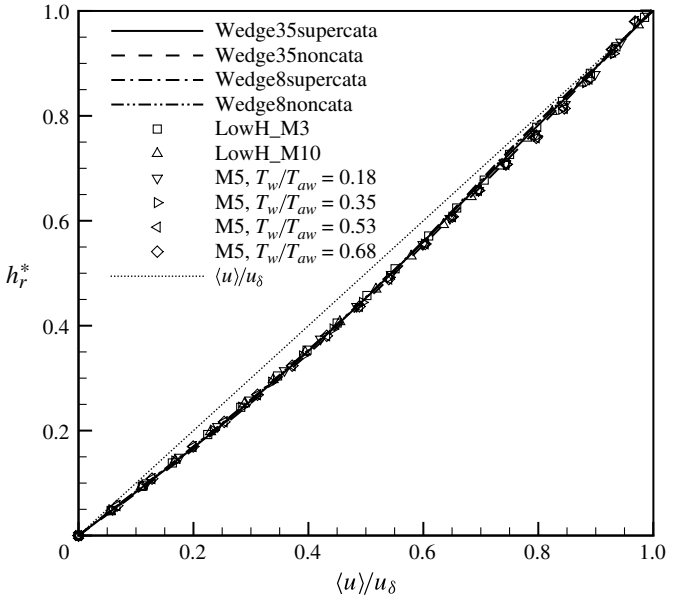

FIGURE 9. Non-dimensional 'recovery enthalpy' $h_r^* = (\tilde{h}_r - h_w)/(h_{aw} - h_w)$ versus $\tilde{u}/u_\delta$ for various DNS data. The Mach 5 data are from DNS by Duan *et al.* (2010).

further reduced to

$$\frac{\tilde{T}}{T_\delta} = \frac{T_w}{T_\delta} + \frac{T_{aw} - T_w}{T_\delta} f\left(\frac{\tilde{u}}{u_\delta}\right) + \frac{T_\delta - T_{aw}}{T_\delta}\left(\frac{\tilde{u}}{u_\delta}\right)^2. \tag{3.6}$$

Equation (3.6) is the same as the Walz's version of the modified Crocco relation (3.2) except that $\tilde{u}/u_\delta$ has been replaced by $f(\tilde{u}/u_\delta)$ in the second term of Walz's relation. For flows with adiabatic or close to adiabatic walls, the influence of the exact functional form of $f(\tilde{u}/u_\delta)$ on temperature–velocity relations diminishes after it is multiplied by $T_{aw} - T_w$, and (3.2) works well, as it is shown in Duan *et al.* (2011), while for flows with non-adiabatic walls, the difference between $f(\tilde{u}/u_\delta)$ and $(\tilde{u}/u_\delta)$ causes significant deviation from (3.2), as shown in figure 8 and in Duan *et al.* (2010).

3.2. *Turbulence quantities*

Figure 10 plots turbulence intensities and density-weighted intensities in streamwise, spanwise and wall-normal directions across boundary layers for various enthalpy cases. The incompressible data of Spalart (1988) are also plotted. The intensity profiles have similar shapes with approximately consistent maxima between corresponding high- and low-enthalpy cases. The density-weighted data bring the magnitude of the compressible extrema closer to the incompressible case. A similar trend is observed for the Reynolds shear stress, as shown in figure 11.

The density-weighted intensities and Reynolds shear stress for cases Wedge8supercata and Wedge8noncata exhibit a plateau around the extrema, while for other enthalpy cases and the incompressible data, the peak is much sharper. Cases Wedge8supercata and Wedge8noncata have the strongest 'real-gas' effects, as indicated by the large deviation in specific heat ratio from the perfect gas value 1.4 in figure 4(*a*). Real-gas effects allow the reallocation of energy from the flow into the internal structure of air molecules, resulting in less severe gradients of mean

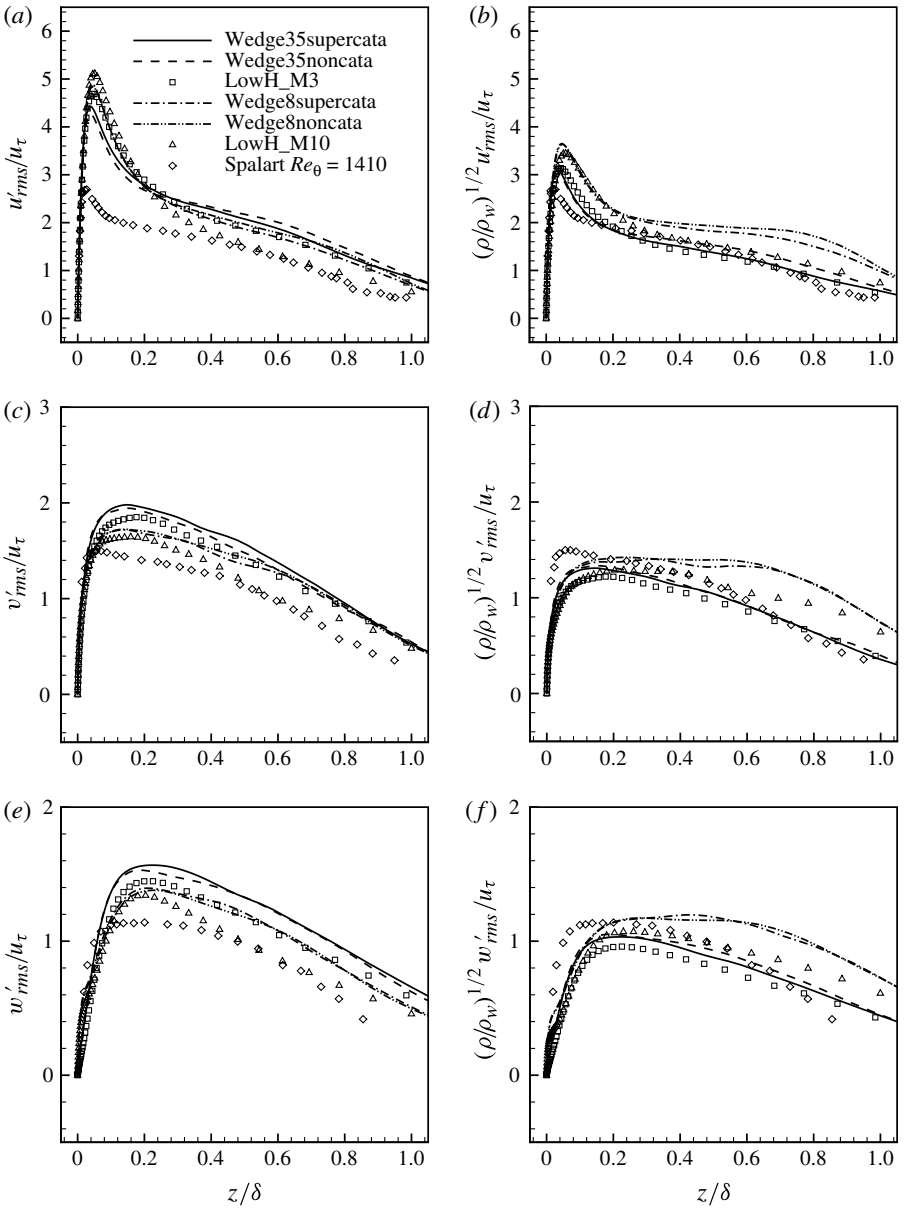

FIGURE 10. Turbulence intensities and density-weighted turbulence intensities in (*a*,*b*) streamwise, (*c*,*d*) spanwise, (*e*,*f*) wall-normal directions across boundary layers for various enthalpy cases.

temperature and density across the boundary layer, as shown in figure 12. The intensity profiles weighted by the more uniform mean density profile would tend to make a plateau.

Figure 13 plots the normalized Reynolds heat flux. Following the gradient transport assumption, the shape of the Reynolds heat flux profiles is closely related to the sign and magnitude of the wall-normal gradient of mean temperature. For all cases, the

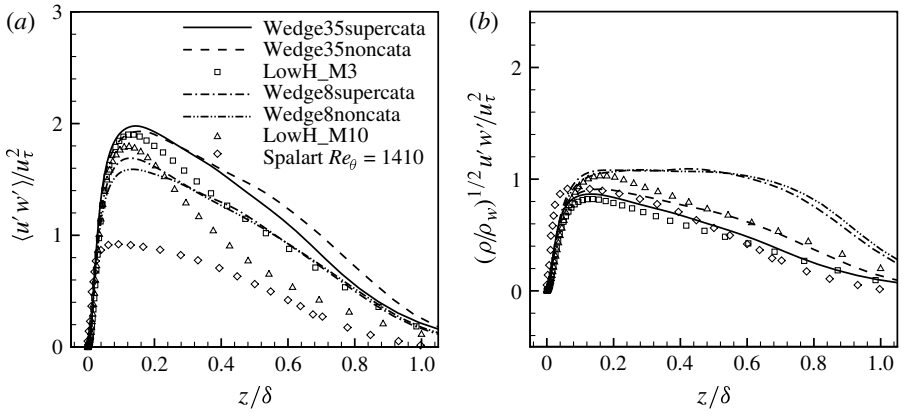

FIGURE 11. $-\overline{u'w'}$ versus z/δ, (*a*) scaled by $1/u_\tau^2$ and (*b*) scaled by $(\overline{\rho}/\overline{\rho}_w)/u_\tau^2$.

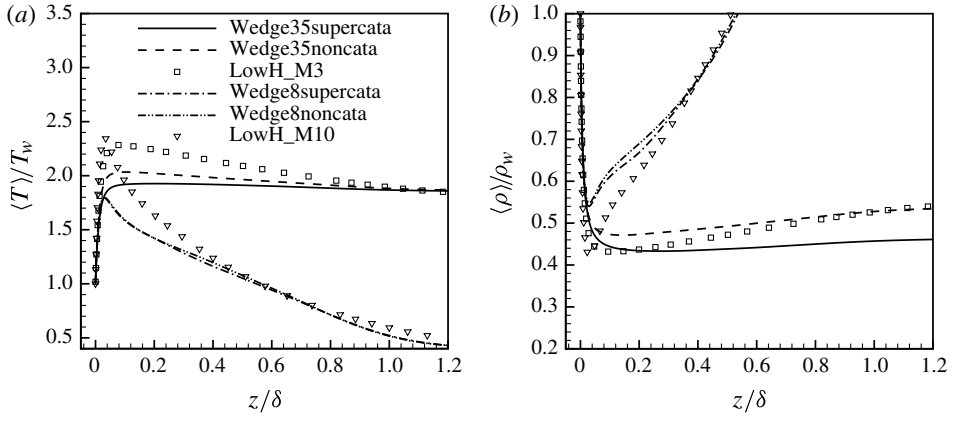

FIGURE 12. Profiles for (*a*) mean temperature and (*b*) mean density for various enthalpy cases.

crossover location, where $\overline{\rho w'' T''} = 0$, nearly coincides with the location of maximum mean temperature, or the location where $\partial \tilde{T}/\partial z = 0$, which is shown in figure 17.

In terms of fluctuations in thermodynamic quantities, figure 14(*a*,*b*) plots r.m.s. values of pressure fluctuation normalized by $\overline{p}_w$ and $\overline{\rho}_w u_\tau^2$, respectively. It is shown that the high-enthalpy cases have larger amplitude of pressure fluctuations than the corresponding low-enthalpy cases for both conditions. The thermal and chemical relaxations for flows with 'real-gas' effects increase the 'capacitance' of the fluid medium and thus result in lower speed of sound than the otherwise frozen flow at the same condition, which in turn increases the turbulent Mach number (figure 22) and pressure fluctuation level, as in figure 14(*a*,*b*). Figure 15(*a*,*b*) plots $\rho'_{rms}/\bar{\rho}$ and $T'_{rms}/\bar{T}$, showing the combined influence of 'real-gas' effects on the mean and r.m.s. profiles.

4. Skin friction and heat transfer

For high-enthalpy flows, the heat transfer to a surface is composed of the usual conduction term plus an additional term, which results from the diffusion of species to

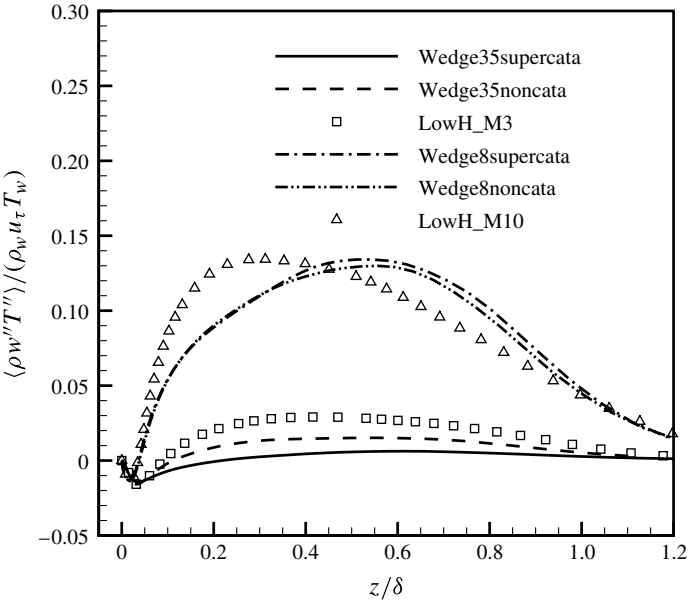

FIGURE 13. Normalized Reynolds heat flux $\overline{\rho w'' T''}/(\overline{\rho} u_\tau \tilde{T}_w)$ for various cases.

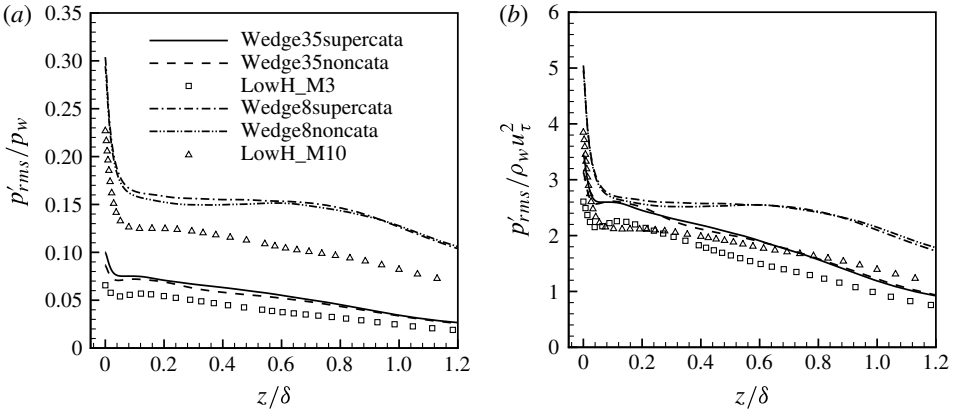

FIGURE 14. p'_{rms} versus z/δ, (*a*) scaled by $1/\overline{p}_w$ and (*b*) scaled by $1/\overline{\rho}_w u_\tau^2$.

the surface and depends on the surface catalytic property. We can write this as

$$q_w = q_{cond} + q_{cata} = \kappa \frac{\partial T}{\partial z} + \sum_{s=1}^{ns} \beta_s h_s^\circ J_s, \tag{4.1}$$

where β_s is the chemical energy accommodation coefficient, which is the ratio of chemical energy transferred to the surface compared to the available energy from recombination and is taken to be unity in the current simulations, and h_s° is the species enthalpy of formation. The value of q_{cata} is non-zero only if the flow is chemically reacting and the surface is catalytic. The Stanton number C_h and the skin friction

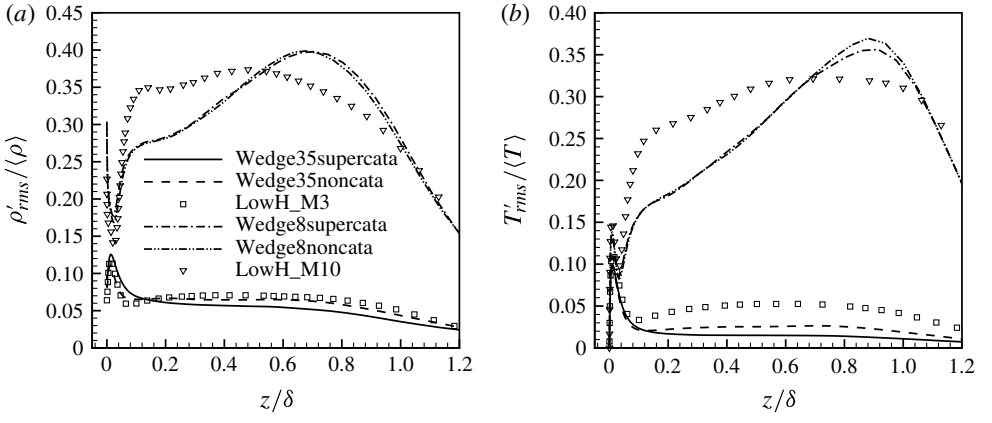

FIGURE 15. (*a*) $\rho'_{rms}/\overline{\rho}$ and (*b*) $T'_{rms}/\overline{T}$ versus z/δ for cases Wedge35 and Wedge8.

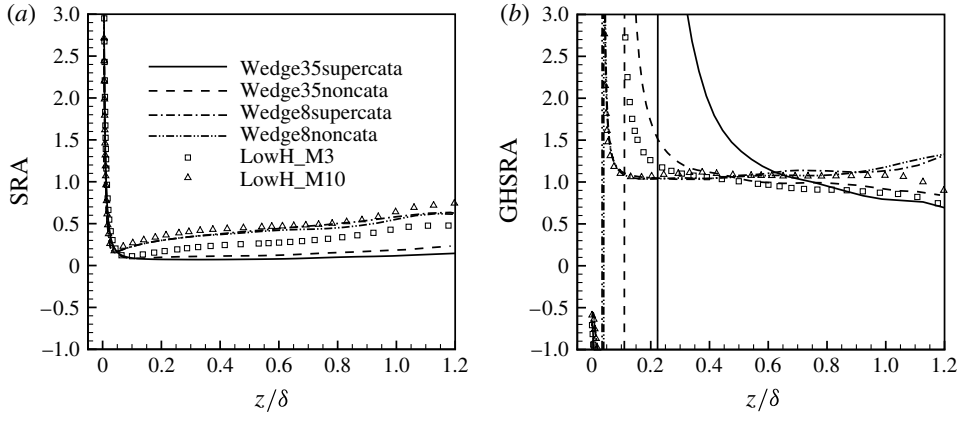

FIGURE 16. Plot of (*a*) the strong Reynolds analogy, as expressed by (5.1), and (*b*) generalized Huang's version of the modified Reynolds analogy, as expressed by (5.5) for various cases.

coefficient are defined as

$$C_h = \frac{q_w}{\rho_\delta u_\delta (h_{aw} - h_w)}, \quad C_f = \frac{\tau_w}{\frac{1}{2}\rho_\delta u_\delta^2}. \tag{4.2}$$

The Reynolds analogy factor is defined as

$$R_{af} = \frac{2C_h}{C_f} = \frac{u_\delta q_w}{\tau_w (h_{aw} - h_w)}. \tag{4.3}$$

Table 4 gives the DNS calculated skin friction, Stanton number, and Reynolds analogy factor as well as the skin friction predicted by the van-Driest II theory (van Driest 1956). It is shown that the van-Driest II theory predicts the DNS results within approximately 10 %.

Both C_f and C_h increase slightly with increasing flow enthalpy, but the ratio remains nearly constant, as indicated by R_{af}, which has value of approximately 1.2 for all cases. For comparison, the low-enthalpy, hypersonic experimental data on smooth flat

Case	C_f	$(C_f)_{VanDriestII}$	C_h	$2C_h/C_f$	$\overline{q}_{w,cata}/\overline{q}_w$	$\tau'_{w,rms}/\overline{\tau_w}$	$q'_{w,rms}/\overline{q}_w$
Wedge35supercata	3.78×10^{-3}	3.62×10^{-3}	2.24×10^{-3}	1.19	0.30	0.45	0.45
Wedge35noncata	3.61×10^{-3}	3.59×10^{-3}	2.11×10^{-3}	1.17	0.00	0.43	0.52
Wedge8supercata	1.02×10^{-3}	8.92×10^{-4}	6.13×10^{-4}	1.20	0.05	0.55	0.66
Wedge8noncata	9.68×10^{-4}	8.49×10^{-4}	5.84×10^{-4}	1.21	0.00	0.55	0.68
LowH_M3	3.12×10^{-3}	3.56×10^{-3}	1.82×10^{-3}	1.17	0.00	0.42	0.43
LowH_M10	1.04×10^{-3}	1.09×10^{-3}	6.11×10^{-4}	1.18	0.00	0.49	0.55

TABLE 4. Skin friction and heat transfer for the DNS data.

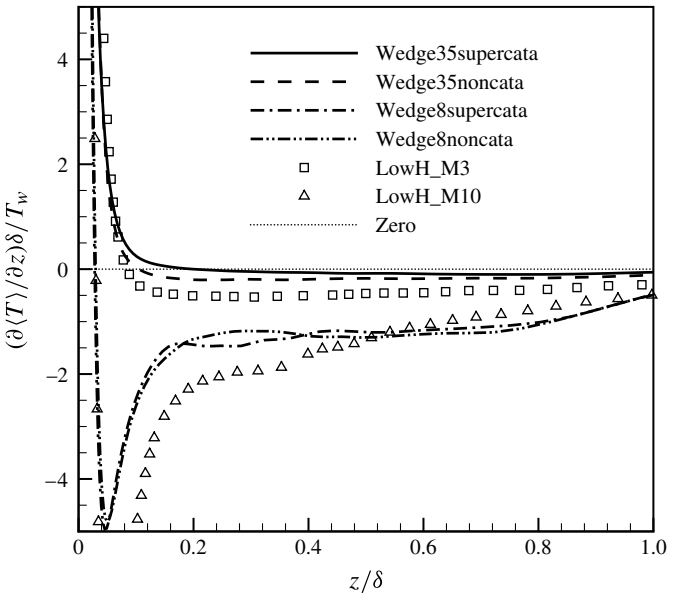

FIGURE 17. Normalized mean static temperature gradient $(\delta/\tilde{T}_w)(\partial\tilde{T}/\partial z)$ for various enthalpy cases. Dotted line represents the zero value.

plates by Hopkins & Inouye (1971) and Keener & Polek (1972), which have edge Mach number varying from 4.9 to 7.8, and T_{aw}/T_w from 0.3 to 0.5, indicate that $0.9 < R_{af} < 1.3$, as reviewed by Roy & Blottner (2006).

Wall catalysis increases C_h under both high-enthalpy conditions, and catalytic heating can be a significant portion of total heating when the flow is significantly dissociated, as is shown for the case Wedge35supercata. For all cases, significant fluctuations exist (>40 % relative to the mean) for both τ_w and q_w.

5. Reynolds analogies

Morkovin (1962) proposed five SRA relations. Three of them are as follows:

$$\frac{T''_{rms}/\tilde{T}}{(\gamma-1)M_a{}^2(u''_{rms}/\tilde{u})} \approx 1, \tag{5.1}$$

$$-R_{u''T''} \approx 1, \tag{5.2}$$

$$Pr_t = \frac{\overline{\rho u''w''}(\partial\tilde{T}/\partial z)}{\overline{\rho w''T''}(\partial\tilde{u}/\partial z)} \approx 1. \tag{5.3}$$

Figure 16(*a*) plots the relationship between r.m.s. temperature and streamwise velocity fluctuations, as expressed by (5.1). Equation (5.1) fails to account for the heat flux at the wall and does not match the DNS data.

Several 'modified' forms of the strong Reynolds analogy have been proposed to account for the heat flux at the wall and remove its wall temperature dependence. For example, Cebeci & Smith (1974) derived an extended form. More recently, Gaviglio (1987), Rubesin (1990), and Huang, Coleman & Bradshaw (1995) presented modified

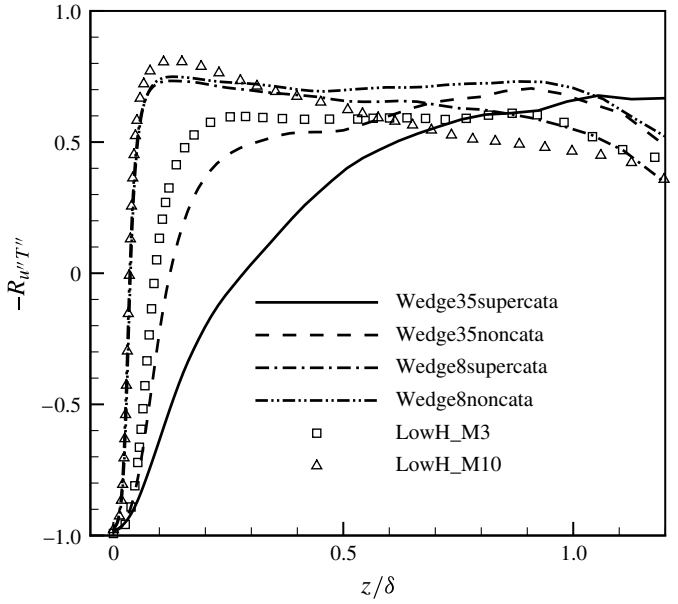

FIGURE 18. $-R_{u''T''}$ for various enthalpy cases.

Reynolds analogies (GSRA, RSRA and HSRA, respectively) which have the form

$$\frac{T''_{rms}/\tilde{T}}{(\gamma-1)M_a{}^2(u''_{rms}/\tilde{u})} \approx \frac{1}{c(1-(\partial\tilde{T}_t/\partial\tilde{T}))}, \tag{5.4}$$

with $c = 1.0$, $c = 1.34$ and $c = Pr_t$, respectively. Low-enthalpy DNS data have shown that HSRA performs best for both adiabatic and non-adiabatic turbulent boundary layers (Guarini *et al.* 2000; Maeder *et al.* 2001; Duan *et al.* 2010, 2011). However, HSRA is derived assuming calorically perfect gas. By removing this assumption, a generalized form of HSRA can be derived:

$$T''_{rms} = -\frac{1}{Pr_t}\frac{\partial\tilde{T}}{\partial\tilde{u}}u''_{rms}. \tag{5.5}$$

We refer to (5.5) as GHSRA. A cursory description of this generalization is given in the Appendix.

Figure 16(*b*) plots the ratio of the left-hand side of (5.5) to its right-hand side for various enthalpy cases. The validity of GHSRA depends critically on the peak location of $\tilde{T}$, or the crossover location, where $\partial\tilde{T}/\partial z = 0$ (figure 17). As the crossover location moves further away from the wall, the validity of GHSRA worsens. At $\partial\tilde{T}/\partial z \approx 0$, the 'mixing length' assumption, where $l_T = T''_{rms}/(\partial\tilde{T}/\partial z)$, no longer holds and GHSRA fails.

Figure 18 plots the correlation between temperature and velocity fluctuations across the boundary layer for various enthalpy cases. It is shown that in the outer part of the boundary layer, u'' and T'' are not perfectly anti-correlated for all enthalpy cases and $-R_{u''T''}$ is around 0.7, similar to the results reported by Guarini *et al.* (2000), Maeder *et al.* (2001), Martín (2007) and Duan *et al.* (2010, 2011). The major enthalpy dependence for the correlation coefficient happens in the region close to the wall, where u'' and T'' have a positive correlation. Similar to GHSRA, the crossover location,

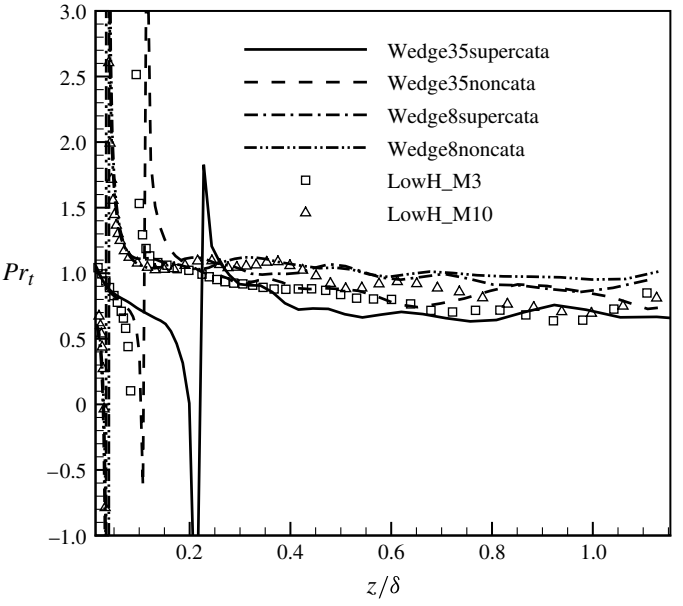

FIGURE 19. Pr_t for various cases.

where $-R_{u''T''} = 0$, nearly coincides with the location of maximum mean temperature. The sign of $R_{u''T''}$ depends on that of the local mean temperature gradient. Ejection and sweep events give a negative and positive value of u'', respectively, but the sign of T'' is influenced by the sign of the mean temperature gradient. For ejections and sweeps, T'' is negative and positive, respectively, if the gradient of mean temperature is positive. As a result, $-R_{u''T''}$ is negative if the gradient of mean temperature is positive, positive if the gradient of mean temperature is negative, and zero if the gradient of mean temperature is zero, which is the location of maximum mean temperature. Similar phenomena of positive near-wall correlations are found in DNS of strongly cooled channel flow (Coleman, Kim & Moser 1995) and boundary layers (Duan *et al.* 2010).

Figure 19 plots the turbulent Prandtl number across the boundary layer. Pr_t is relatively insensitive to flow enthalpy conditions and is close to unity in the outer part of the boundary layer. In addition, there exist regions of overshoot and sign change, which coincide with the zero crossover location of Reynolds heat flux $\overline{\rho w''T''}$ (figure 13) and $\partial\tilde{T}/\partial z$ (figure 17).

6. Gradient transport assumption

In order to close the averaged governing equations in RANS calculations of chemically reacting turbulent boundary layers, modelling of the Reynolds flux terms $\overline{\rho u_i'' h''}$ and $\overline{\rho u_i'' Y_s''}$ is required, in addition to the Reynolds stress $\overline{\rho u_i'' u_j''}$.

With the gradient transport assumption, the Reynolds flux term for a flow property ϕ, after assuming homogeneity in the streamwise and spanwise directions, can be expressed as

$$-\overline{\rho w''\phi''} = \frac{\mu_T}{\sigma_\phi}\frac{\partial\tilde{\phi}}{\partial z}, \tag{6.1}$$

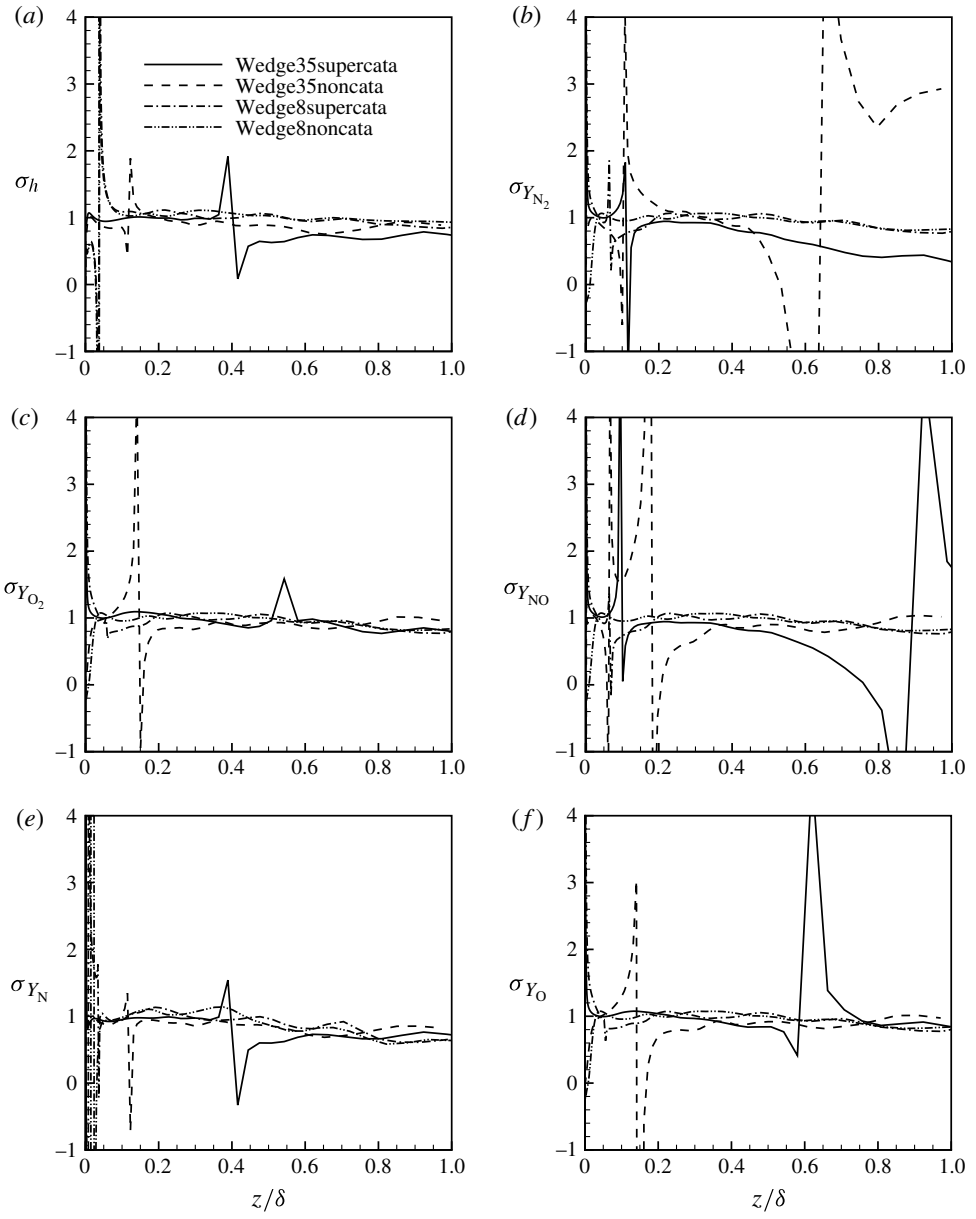

FIGURE 20. (*a*) σ_h; (*b*) $\sigma_{Y_{N_2}}$; (*c*) $\sigma_{Y_{O_2}}$; (*d*) $\sigma_{Y_{NO}}$; (*e*) σ_{Y_N}; (*f*) σ_{Y_O}.

where μ_T is the turbulent viscosity defined by

$$-\overline{\rho u'' w''} = \mu_T \frac{\partial \tilde{u}}{\partial z}; \tag{6.2}$$

σ_ϕ is the turbulent Prandtl number when ϕ stands for enthalpy h, and the turbulent Schmidt number when ϕ is species mass fraction Y_s.

While the specification of μ_T has been discussed extensively in the turbulence modelling community (Wilcox 2006), σ_ϕ is commonly treated as an empirical constant, without much justification, especially under hypersonic conditions. Figure 20 plots the

turbulent Prandtl number σ_h as well as the turbulent Schmidt number σ_{Y_s} across the boundary layer for various high-enthalpy cases. It is shown that for all cases σ_ϕ is close to unity for most of the boundary layers. Similar to figure 19, there exist regions of overshoot and abrupt sign change in the values of σ_ϕ, which coincide with the location where $\overline{\rho w'' \phi''} \approx 0$ or $\partial\tilde{\phi}/\partial z \approx 0$.

7. Turbulent kinetic energy budget

The turbulent kinetic energy (TKE) is defined as

$$\tilde{k} = \frac{1}{2}\frac{\overline{\rho u_i'' u_i''}}{\overline{\rho}} \tag{7.1}$$

and the budget equation for turbulent kinetic energy is, after assuming homogeneity in streamwise and spanwise directions, given by

$$\frac{\partial}{\partial t}(\overline{\rho}\tilde{k}) + \tilde{w}\frac{\partial}{\partial z}(\overline{\rho}\tilde{k}) = P + T + \Pi + \phi_{dif} + \phi_{dis} + ST, \tag{7.2}$$

where

$$P = -\overline{\rho u_i'' w''}\frac{\partial \tilde{u}_i}{\partial z}, \tag{7.3}$$

$$T = -\frac{1}{2}\frac{\partial}{\partial z}\overline{\rho u_i'' u_i'' w''}, \tag{7.4}$$

$$\Pi = \Pi_t + \Pi_d = -\frac{\partial}{\partial z}\overline{w'' p'} + \overline{p'\frac{\partial u_i''}{\partial x_i}}, \tag{7.5}$$

$$\phi_{dif} = \frac{\partial}{\partial z}\overline{u_i'' \tau_{iz}'}, \tag{7.6}$$

$$\phi_{dis} = -\overline{\tau_{ij}'\frac{\partial u_i''}{\partial x_j}}, \tag{7.7}$$

$$ST = -\overline{w''}\frac{\partial \overline{p}}{\partial z} + \overline{u_i''}\frac{\partial \overline{\tau_{ij}}}{\partial x_j} - \overline{\rho}\tilde{k}\frac{\partial \tilde{w}}{\partial z}. \tag{7.8}$$

The terms in (7.2) can be interpreted as follows: the left-hand side is the substantial derivative of the turbulent kinetic energy along a mean streamline; P is the rate of production of turbulent kinetic energy due to mean velocity gradient; T is turbulent transport; Π includes the pressure terms (pressure diffusion and the pressure dilatation, respectively); ϕ_{dif} is the viscous diffusion; ϕ_{dis} is the viscous dissipation; and ST represents terms that arise when the density is not constant. The first two appear due to the difference between the Favre and Reynolds averaging and the third term is the production term due to dilatation. Besides terms in ST, pressure dilatation as well as dilatational dissipation are also due to non-constant density.

Figure 21(*a–d*) plots the terms in the budget of turbulent kinetic energy for various enthalpy conditions, normalized by conventional wall variables (defined in terms of the mean density, viscosity and shear stress at the wall) and 'semi-local' scaling (Huang *et al.* 1995) (replacing $\overline{\rho}_w$ with $\overline{\rho}(z)$, u_τ with $u_\tau^* \equiv \sqrt{\tau_w/\overline{\rho}(z)}$, and $z_\tau^* \equiv \overline{\mu}(z)/(\overline{\rho}(z)u_\tau^*)$), respectively. Pressure terms and ST are small and have not been included on the plot. It is shown that wall catalysis conditions have a subtle influence on budget terms for both Wedge35 and Wedge8. Wall units do not collapse the budget terms at different

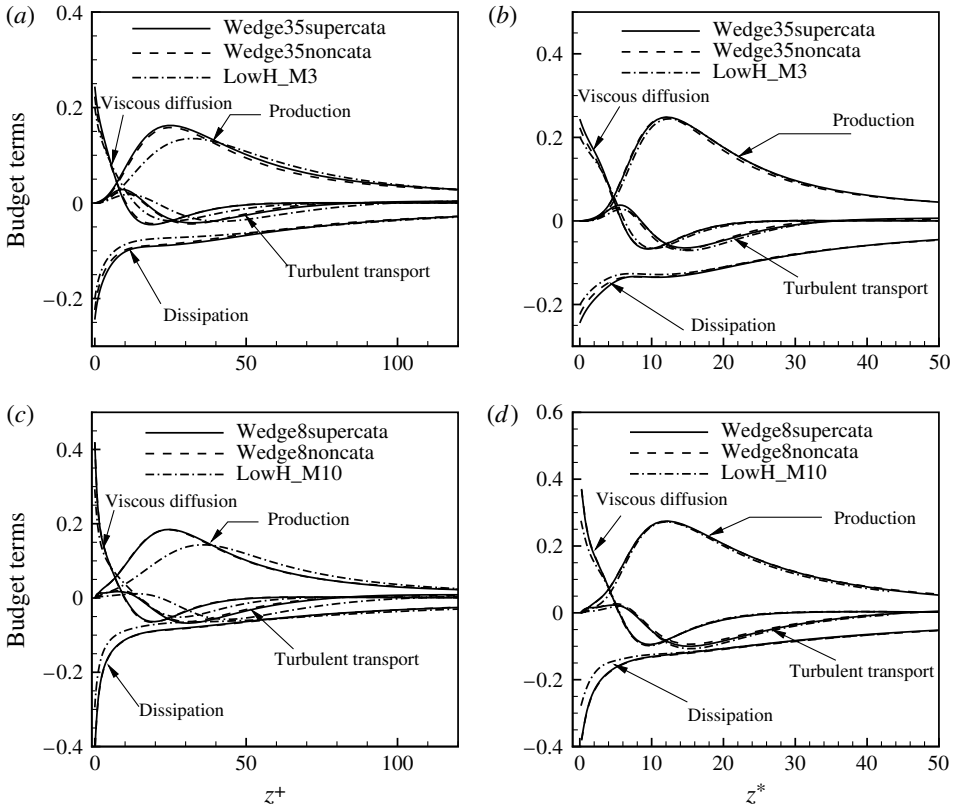

FIGURE 21. Turbulent kinetic energy budget for cases Wedge35 and Wedge8, non-dimensionalized with (*a*,*c*) wall units, and (*b*,*d*) semi-local units, respectively. Variables in wall units are normalized by $\overline{\rho}_w u_\tau^3/z_\tau$ and $z^+ = z/z_\tau$; variables in semi-local units are normalized by $\overline{\rho} u_\tau^{*3}/z_\tau^*$ and $z^* = z/z_\tau^*$.

enthalpy conditions. The magnitude of TKE budget terms decreases with decreasing enthalpy conditions, and the maximum values shift farther away from the wall. When the high- and low-enthalpy data are scaled with 'semi-local' scaling, the data collapse, as has also been observed in Duan *et al.* (2010).

8. Compressibility effects

8.1. *Turbulent Mach number*

An indicator for the significance of compressibility effects is the turbulent Mach number, defined by

$$M_t = \frac{(\overline{u_i'u_i'})^{1/2}}{\overline{a}}. \tag{8.1}$$

It is shown in figure 22(*a*) that the magnitude of M_t is significantly larger for Wedge8 than Wedge35 due to the larger edge Mach number. The wall catalysis conditions have a subtle influence on M_t for both conditions. The high-enthalpy cases have larger values of M_t than the low-enthalpy cases, since the thermal and chemical relaxations in high-enthalpy flow lower the specific heat ratio and result in lower speed of sound. However, the same trend is not observed for M'_{rms}, which is the r.m.s. fluctuation of the Mach number and thereby includes temperature fluctuations,

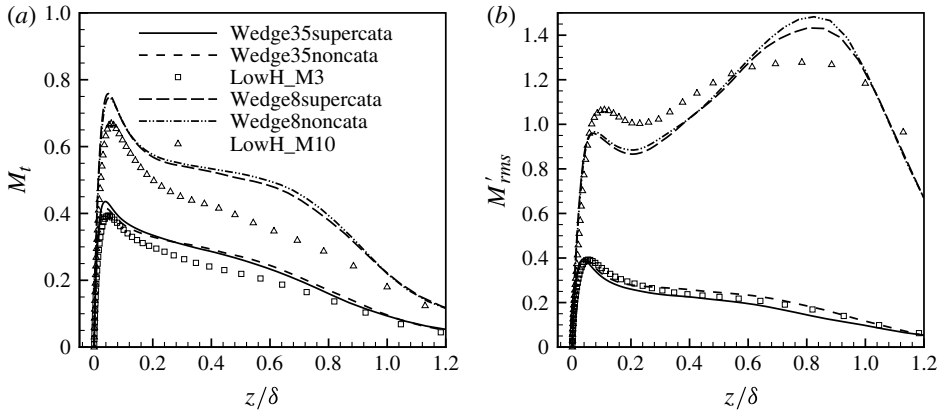

FIGURE 22. Simulation results of (*a*) turbulence Mach number and (*b*) fluctuating Mach number for various cases.

as shown in figure 22(*b*). The relatively higher temperature fluctuations in the low-enthalpy conditions (figure 15*b*) result in regions of larger values of M'_{rms} for the low-enthalpy cases.

It is commonly believed that 0.3 is the threshold of M_t above which compressibility effects become important for turbulence behaviour (Smits & Dussauge 2006). The relatively large values of M_t and M'_{rms} for all cases might indicate the significance of compressibility effects. The effect of compressibility can be sought by investigating explicit dilatation terms that arise from the non-vanishing velocity divergence such as pressure dilatation and dilatational dissipation.

8.2. *Pressure dilatation and pressure–strain terms*

One of the terms arising from the non-vanishing velocity divergence is the pressure dilatation term. Figure 23(*a*) plots the pressure dilatation term $\Pi_d = \overline{p'(\partial u''_i/\partial x_i)}$ for various cases. To illustrate the relative importance of Π_d compared to relevant terms in the TKE budget, Π_d is normalized by the corresponding production term $P = -\overline{\rho u''_i w''}(\partial \tilde{u}_i/\partial z)$ in each case. It is shown that the relative importance of Π_d does not change significantly with wall catalysis and enthalpy conditions, and the pressure dilatation term is small relative to the production term through most of the boundary layers, with maximum ratio less than 5 % for $0 < z/\delta < 0.8$. The ratio goes up significantly near the boundary layer edge, due to the production term nearing zero.

In a study of compressible mixing layers, Vreman, Sandham & Luo (1996) found that the effect of compressibility is to change the structure of the pressure field, which results in the modification of the Reynolds stress anisotropy. Figure 23(*b*) plots the pressure–strain term $\Pi_{13} = \overline{p'((\partial u''/\partial z) + (\partial w''/\partial x))}$ normalized by production $P = -\overline{\rho u''_i w''}(\partial \tilde{u}_i/\partial z)$ for various cases. Similar to the pressure dilatation term, the pressure–strain term for boundary layers is insensitive to wall catalysis and enthalpy conditions.

8.3. *Dilatational dissipation*

Another term arising from the non-vanishing velocity divergence is the dilatational dissipation

$$\phi_d = \frac{4}{3}\overline{\mu}\,\overline{\frac{\partial u'_i}{\partial x_i}\frac{\partial u'_k}{\partial x_k}}. \tag{8.2}$$

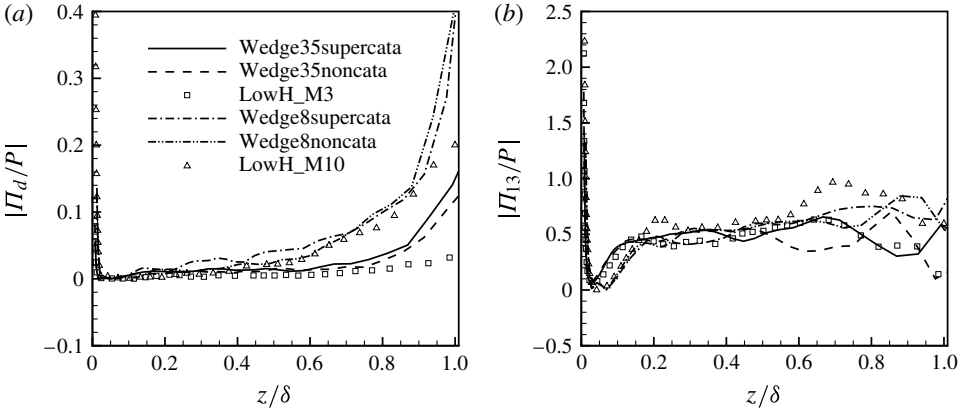

FIGURE 23. (*a*) Pressure dilatation Π_d and (*b*) pressure–strain Π_{13} normalized by production P.

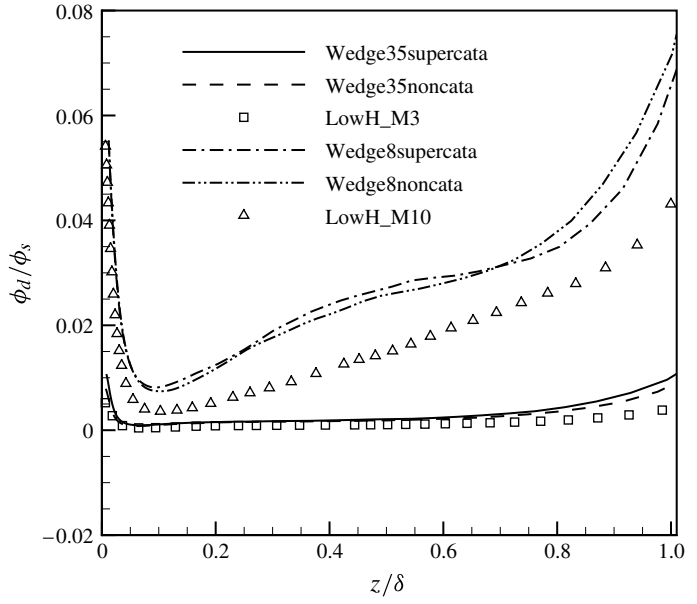

FIGURE 24. ϕ_d/ϕ_s versus distance away from the wall.

The solenoidal dissipation is defined as

$$\phi_s = \overline{\mu}\overline{\omega_i'\omega_i'}, \tag{8.3}$$

where ω is the vorticity.

Figure 24 plots the ratio of ϕ_d to ϕ_s for various cases. It is shown that the ratio is not significantly influenced by the wall catalysis condition, and is somewhat increased with increasing flow enthalpy. For all cases, the ratio remains small with maximum value less than 8 %.

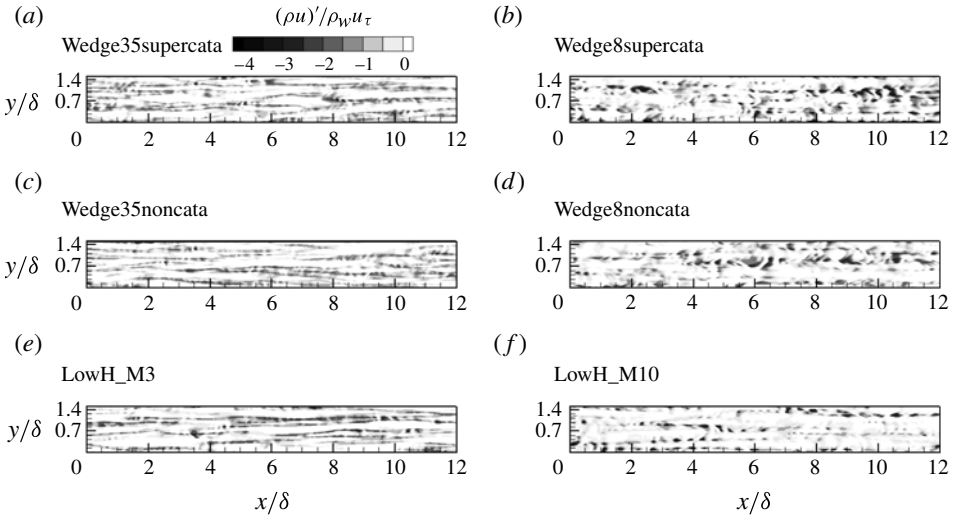

FIGURE 25. Instantaneous flow field at $z^+ = 5$ to visualize near-wall streaks for various cases. Shading shows ρu fluctuations.

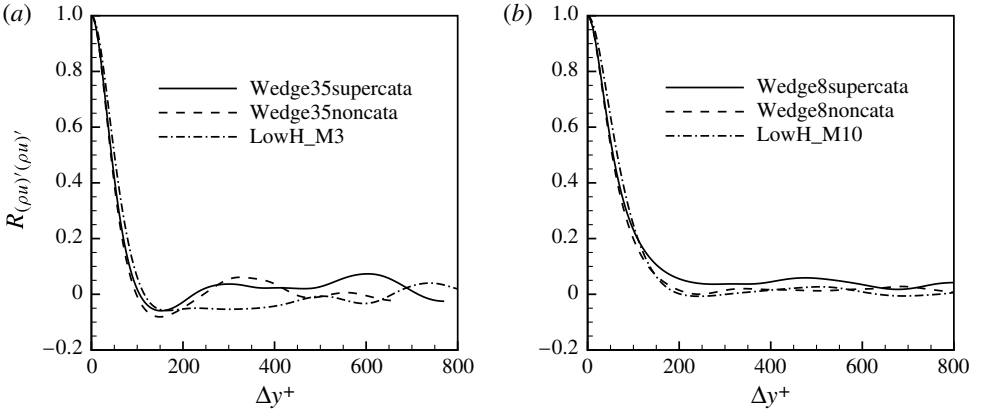

FIGURE 26. Two-point correlation $R_{(\rho u)'(\rho u)'}$ versus Δy^+ at $z^+ = 5$ for various cases.

9. Structure analysis

9.1. *Near-wall streaks*

In this section, we investigate the effects of high-enthalpy on near-wall streaks. Figure 25(*a–f*) plots the instantaneous streamwise mass flux fluctuations at $z^+ = 5$ for various cases. Long regions of negative ρu fluctuation are identified as streaks and are visible in the plots as elongated dark regions. Streaks are present in all cases, and the superficial similarity between the corresponding high- and low-enthalpy cases is apparent. Figure 26 plots the two-point correlation of the streamwise mass flux to demonstrate the influence of enthalpy conditions on the spanwise spacing of near-wall streaks. The small variation in the two-point correlation among different enthalpy cases indicates that the average spanwise spacing is insensitive to wall catalysis and enthalpy conditions.

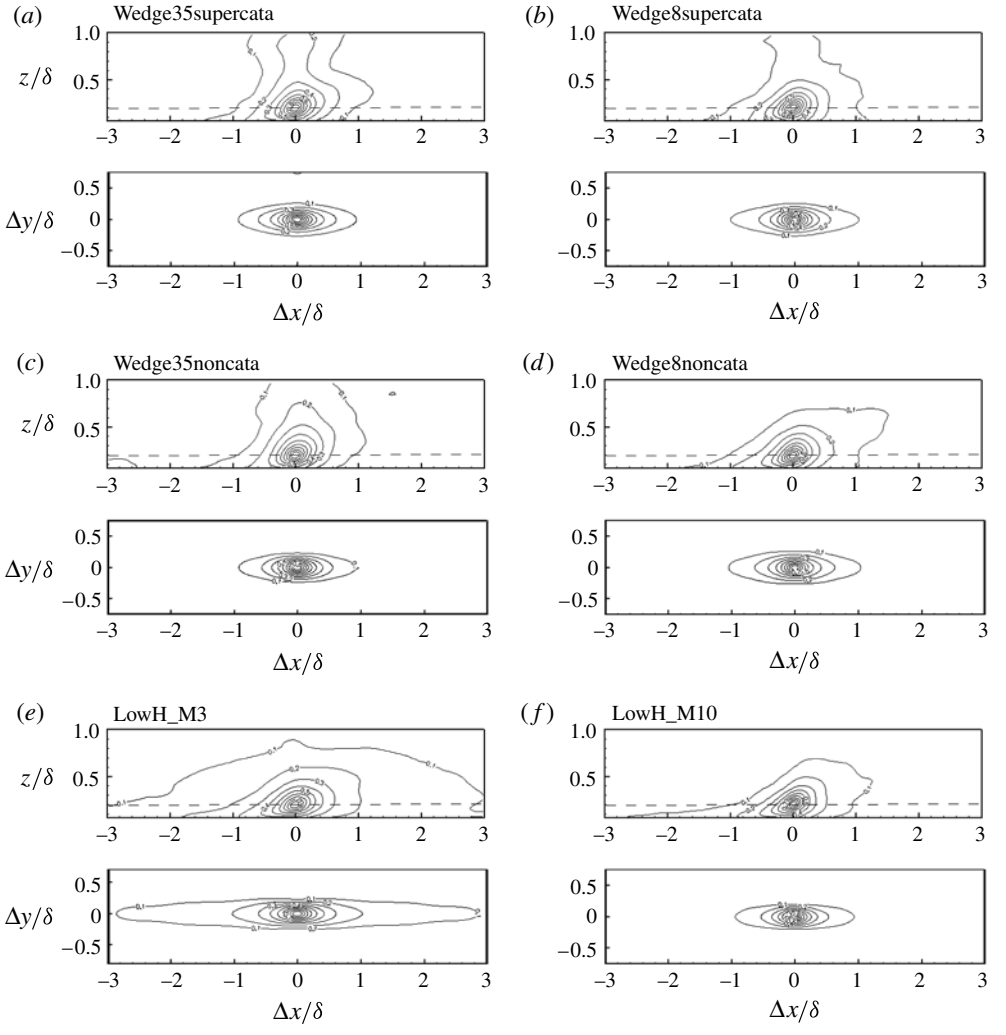

FIGURE 27. Isocorrelation contour maps of $R_{(\rho u)'(\rho u)'}$ for various cases. The dashed line at $z/\delta = 0.2$ in the streamwise/wall-normal plane indicates the wall-normal location of the streamwise/spanwise plane.

9.2. *Outer layer structure*

To investigate the influence of flow enthalpy conditions on the size and inclination angle of the typical eddies, figure 27 plots isocorrelation contour maps in both (x–y) and (x–z) planes for various cases. The contour maps are obtained by fixing 'origin' points at $z/\delta = 0.2$, within the logarithmic layer, and correlating them with neighbouring points lying within either a $6\delta \times 2\delta$ streamwise/spanwise window or a streamwise/wall-normal window spanning 6δ in the streamwise direction and from upper buffer layer to the boundary layer edge in the wall-normal direction. The results are then averaged over all the 'origin' points at $z/\delta = 0.2$ and over all the flow fields. Figure 27 shows that the streamwise and spanwise length scales are approximately 2.0δ and 0.4δ, respectively, at a contour level of 0.1 for all cases except LowH_M3. For the case LowH_M3, the streamwise structure size is significantly elongated, which

might indicate that the flow is more coherent at lower enthalpy. However, similar streamwise elongation is not observed for the case LowH_M10, which might be due to its higher boundary layer edge Mach number, and it has been found by Duan *et al.* (2011) that the structure size decreases significantly with increasing free-stream Mach number. The data indicate that the structures for high-enthalpy cases are more upright than those for the corresponding low-enthalpy cases.

The existence of coherent structures can be further demonstrated by correlating the wall shear stress with the streamwise mass flux (Brown & Thomas 1977; Ringuette, Wu & Martin 2008; O'Farrell & Martín 2009; Duan *et al.* 2010, 2011). The correlation coefficient is defined by

$$R_{\tau_w'(\rho u)'} = \frac{\overline{\tau_w'(x, y)(\rho u)'(x + \Delta x, y + \Delta y, \Delta z)}}{\tau_{w,rms}'(\rho u)_{rms}'}. \tag{9.1}$$

Figure 28 plots the isocorrelation contour maps of $R_{\tau_w'(\rho u)'}$ for various cases in streamwise/wall-normal and streamwise/spanwise planes. The contour plots in the streamwise/wall-normal plane indicate the existence of a downstream leaning structure for all cases, similar to the isocontour maps of $R_{(\rho u)'(\rho u)'}$. In addition, isosurfaces of significant, positive $R_{\tau_w'(\rho u)'}$ can be thought of as surfaces encapsulating the low-momentum fluid in a hairpin packet corresponding to the model of Adrian, Meinhart & Tomkins (2000). Between the legs of a hairpin vortex, the ejection of fluid causes negative $(\rho u)'$ and negative τ_w', thus positive $R_{\tau_w(\rho u)}$. Outside the legs, the sweep events cause positive $(\rho u)'$, which correlates with the negative τ_w' between the legs to give negative $R_{\tau_w(\rho u)}$. Travelling together, multiple vortices form the packet; these coherent vortices act in concert to, on average, create and surround a region of low-momentum fluid. Another noteworthy feature is the existence of a bump in the contour just upstream of $\Delta x/\delta = 0$, corresponding to an increase in $R_{\tau_w(\rho u)}$. This is possible evidence of a younger 'child' hairpin packet, generated through the self-sustaining hairpin process, and streamwise alignment and organization of hairpin packets to form the 'very large-scale motions' of Adrian *et al.* (2000) or the 'superstructures' of Hutchins & Marusic (2007).

The apparent similarity in large-scale motions between high- and low-enthalpy boundary layers can also be found in the structure parameter and intermittency. The 'structure parameter" is defined as $a_1 = -\overline{u'w'}/2\bar{k}$, as plotted in figure 29. For all cases, a_1 is approximately constant in $0.1 < z/\delta < 0.9$, where it assumes values 0.14–0.16. For incompressible boundary layers, a_1 has been found to be approximately constant with values between 0.14 and 0.17 (Smits & Dussauge 2006).

A similar trend is observed for anisotropy ratios v_{rms}'/u_{rms}' and w_{rms}'/u_{rms}', as shown in figure 30(*a*,*b*), and both ratios assume values within the range of incompressible flows. For incompressible boundary layers, v_{rms}'/u_{rms}' has been reported to be nearly constant with values between 0.6 and 0.7, and w_{rms}'/u_{rms}' has been found to assume values varying between 0.4 and 0.8 (Smits & Dussauge 2006).

The intermittency is a measure of the wallward extent of the entrainment of the external, initially irrotational flow by large-scale motions. Figure 31 plots the flatness factor for various cases. It is shown that wall catalysis and enthalpy conditions do not influence intermittency to any significant extent.

10. Conclusion

We perform direct numerical simulations of flat-plate hypersonic turbulent boundary layers at high- and low-enthalpy conditions in air to study the effects of enthalpy

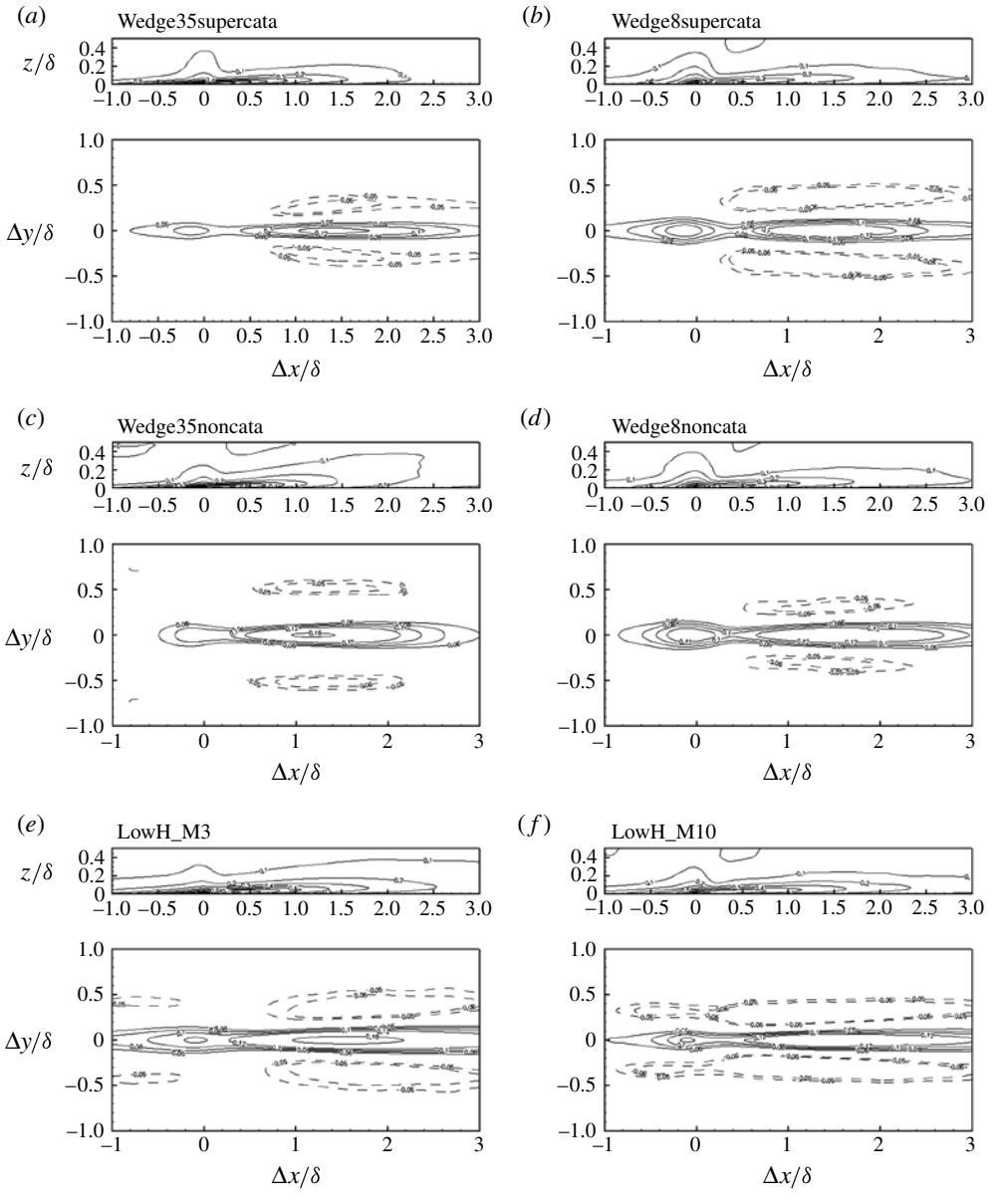

FIGURE 28. Isocorrelation contour maps of $R_{\tau'_w(\rho u)'}$ for various cases. The contour maps in the streamwise/spanwise plane are plotted at $z/\delta = 0.2$ with negative contours drawn as dashed curves.

conditions on boundary layer flow. The enthalpy levels for the high- and low-enthalpy conditions are typical of hypersonic flight and ground-based facilities, respectively. We showed that many of the scaling relations which are derived and validated under low-enthalpy conditions for calorically perfect gas still hold or can be generalized for high-enthalpy flows. In particular, we have shown that the van Driest transformed velocity collapses different flow enthalpy results with incompressible results. It is also shown that the r.m.s. velocity fluctuations of different enthalpy conditions are

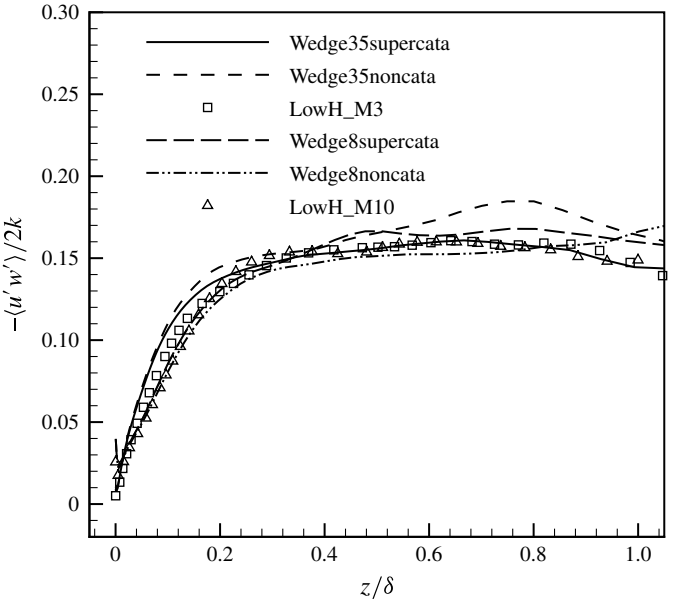

FIGURE 29. Structure parameter $-\overline{u'w'}/2k$ across the boundary layer.

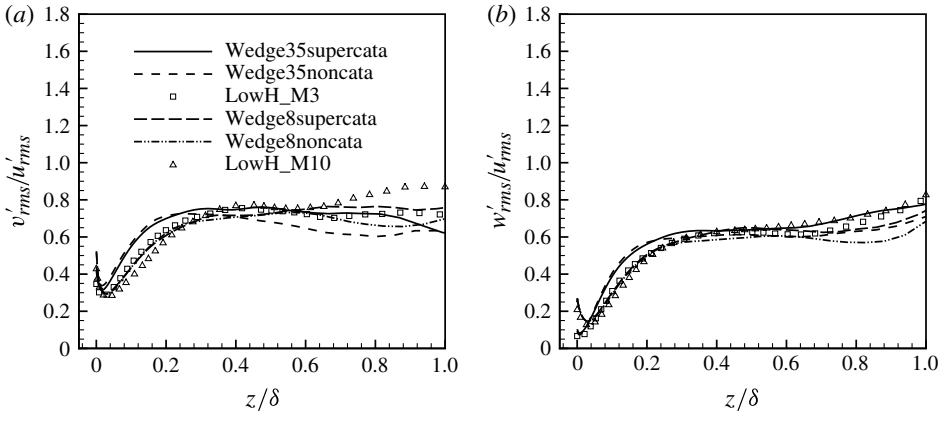

FIGURE 30. Simulation results of (*a*) v'_{rms}/u'_{rms} and (*b*) w'_{rms}/u'_{rms} for various cases.

collapsed by the mean density scaling suggested by Morkovin. While the mean static temperature field no longer exhibits a quadratic dependence upon the mean velocity, as predicted by Walz's version of the modified Crocco relation (3.2), a generalized form of the modified Crocco relation (3.4) which is independent of specific calorical relations can be used to connect the mean temperature with the mean velocity.

In terms of the strong Reynolds analogy, the original SRA relation (Morkovin 1962) breaks down for all enthalpy cases. The generalized Huang's version of the modified SRA (5.5), which removes the calorically perfect gas assumption, provides reasonably good results in the outer part of the boundary layer, with its validity depending critically on the crossover location where $\partial\tilde{T}/\partial z = 0$. We also find that

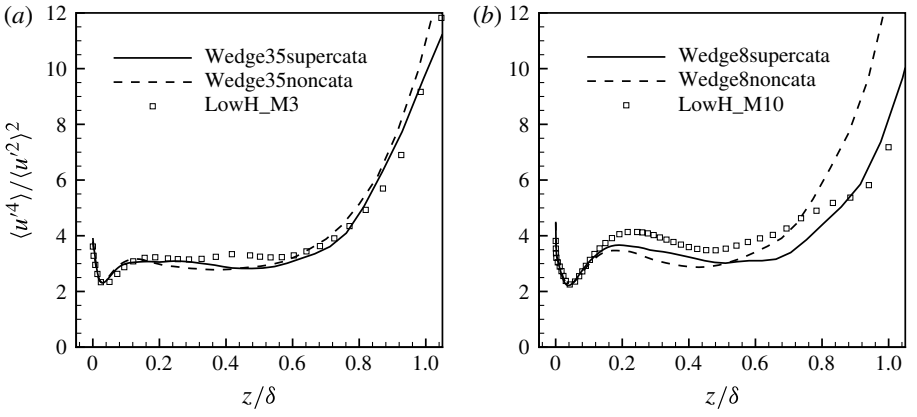

FIGURE 31. Flatness factor versus distance from the wall for various enthalpy cases.

u'' and T'' are not perfectly anti-correlated (as predicted by the SRA, (5.2)) and $-R_{u''T''}$ is approximately 0.7 in the outer part of the boundary layer for different enthalpy cases. The turbulent Prandtl number is nearly constant for most of the boundary layer and insensitive to flow enthalpy conditions. In addition, we find that the gradient transport relation (6.1) works well for various enthalpy cases, and σ_h and σ_Y are approximately one through most of the boundary layer.

In terms of the turbulent kinetic energy budget, we show that the conventional inner scaling does not collapse the data. However, the semi-local scaling that takes into account local variation of fluid properties better collapses the data as found for cold-wall DNS data in Duan *et al.* (2010). The terms arising from the non-vanishing velocity-divergence in TKE budgets, such as pressure dilatation and dilatational dissipation, indicate that direct compressibility effects remain small and insignificant for various enthalpy cases.

Regarding the turbulence structure, we find apparent similarity in the near-wall streaks and large-scale motions between high- and low-enthalpy boundary layers.

The current study describes the characteristics of the high-enthalpy boundary layer flow away from the vicinity of the leading edge, where thermal non-equilibrium is negligible and a fully turbulent boundary layer exists. The results on the turbulence scaling should be of general applicability regardless of the leading-edge flow development.

This work is supported by NASA under Grant NNX08ADO4A.

Appendix

Here, we briefly review the derivation of the modified Reynolds analogy by Gaviglio and Huang *et al.* and generalize it for chemically reacting flows with variable heat capacities.

First, the velocity and temperature fluctuation intensities are related to the 'mixing length scales' (Gaviglio 1987; Huang *et al.* 1995) defined by

$$l_u = u''_{rms}/\partial(\tilde{u}/\partial z), \quad l_T = T''_{rms}/(\partial\tilde{T}/\partial z). \tag{A 1}$$

Gaviglio (1987) assumed $l_u/l_T = 1$, and Huang *et al.* (1995) further showed that $l_u/l_T \approx Pr_t$. With $l_u/l_T \approx Pr_t$, we have

$$T''_{rms} = -\frac{1}{Pr_t}\frac{\partial \tilde{T}}{\partial \tilde{u}} u''_{rms}, \tag{A 2}$$

where the negative sign is due to the opposite signs of $\partial\tilde{u}/\partial z$ and $\partial\tilde{T}/\partial z$ in the outer part of the boundary layer. Equation (A 2) (and also (5.5)) is independent of the calorical relation for the particular fluid, and is therefore more general than HSRA.

By assuming calorically perfect gas, (5.4) can be recovered. Namely, HSRA can be recovered by applying the definition of total temperature T_t with the form

$$h_t = C_p T_t = C_p T + \tfrac{1}{2} u_i u_i \tag{A 3}$$

so that

$$\frac{\partial \tilde{u}}{\partial \tilde{T}} \approx (\partial \tilde{T}_t/\partial \tilde{T} - 1) C_p/\tilde{u}. \tag{A 4}$$

For high-enthalpy flow, C_p is a function of flow temperature and species composition, and the relation (A 3) is no longer valid. As a result, the more general relation (5.5), GHSRA, must be used to relate mean velocity and temperature.

REFERENCES

ADRIAN, R., MEINHART, C. & TOMKINS, C. 2000 Vortex organization in the outer region of the turbulent boundary layer. *J. Fluid Mech.* **422**, 1–54.

BRADSHAW, P. 1977 Compressible turbulent shear layers. *Annu. Rev. Fluid Mech.* **9**, 33–54.

BROWN, G. L. & THOMAS, A. S. W. 1977 Large structure in a turbulent boundary layer. *Phys. Fluids* **20** (10), S243–S252.

CEBECI, T. & SMITH, A. M. O. 1974 *Analysis of Turbulent Boundary Layers*. Academic.

COLEMAN, G. N., KIM, J. & MOSER, R. D. 1995 A numerical study of turbulent supersonic isothermal-wall channel flow. *J. Fluid Mech.* **305**, 159–183.

DONG, M. & ZHOU, H. 2010 The improvement of turbulence modeling for the aerothermal computation of hypersonic turbulent boundary layers. *Sci. Chin.* **53**, 369–379.

VAN DRIEST, E. R. 1956 The problem of aerodynamic heating. *Aeronaut. Engng Rev.* **15** (10), 26–41.

DUAN, L., BEEKMAN, I. & MARTÍN, M. P. 2010 Direct numerical simulation of hypersonic turbulent boundary layers. Part 2. Effect of wall temperature. *J. Fluid Mech.* **655**, 419–445.

DUAN, L., BEEKMAN, I. & MARTÍN, M. P. 2011 Direct numerical simulation of hypersonic turbulent boundary layers. Part 3. Effect of Mach number. *J. Fluid Mech.* **672**, 245–267.

DUAN, L. & MARTÍN, M.P. 2009*a* Effect of finite-rate chemical reactions on turbulence in hypersonic turbulent boundary layers. *AIAA Paper* 2009-0588.

DUAN, L. & MARTÍN, M. P. 2009*b* Effect of turbulence fluctuations on surface heating rate in hypersonic turbulent boundary layers. *AIAA Paper* 2009-4040.

DUAN, L. & MARTÍN, M. P. 2009*c* An effective procedure for testing the validity of DNS of wall-bounded turbulence including finite-rate reactions. *AIAA J.* **47** (1), 244–251.

DUAN, L. & MARTÍN, M. P. 2011 Assessment of turbulence–chemistry interaction in hypersonic turbulent boundary layers. *AIAA J.* **49** (1), 172–184.

GAVIGLIO, J. 1987 Reynolds analogies and experimental study of heat transfer in the supersonic boundary layer. *Intl J. Heat Mass Transfer* **30** (5), 911–926.

GORDON, S. & MCBRIDE, B. J. 1994 Computer program for calculation of complex chemical equilibrium compositions and applications. *NASA RP* 1311.

GUARINI, S. E., MOSER, R. D., SHARIFF, K. & WRAY, A. 2000 Direct numerical simulation of a supersonic turbulent boundary layer at Mach 2.5. *J. Fluid Mech.* **414**, 1–33.

GUPTA, R. N., YOS, J. M., THOMPSON, R. A. & LEE, K. P. 1990 A review of reaction rates and thermodynamic and transport properties for 11-species air model for chemical and thermal non-equilibrium calculations to 30 000 K. *NASA RP* 1232.

HOPKINS, E. J. & INOUYE, M. 1971 Evaluation of theories for predicting turbulent skin friction and heat transfer on flat plates at supersonic and hypersonic mach numbers. *AIAA J.* **9** (6), 993–1003.

HUANG, P. G., COLEMAN, G. N. & BRADSHAW, P. 1995 Compressible turbulent channel flows: DNS results and modelling. *J. Fluid Mech.* **305**, 185–218.

HUTCHINS, N. & MARUSIC, I. 2007 Evidence of very long meandering features in the logarithmic region of turbulent boundary layers. *J. Fluid Mech.* **579**, 1–28.

KEENER, E. R. & POLEK, T. E. 1972 Measurements of Reynolds analogy for a hypersonic turbulent boundary layer on a nonadiabatic flat plate. *AIAA J.* **10** (6), 845–846.

KEYES, F. G. 1951 A summary of viscosity and heat-conduction data for He, H_2, O_2, CO, CO_2, H_2O and air. *Trans. ASME* 589–596.

MAEDER, T. 2000 Numerical investigation of supersonic turbulent boundary layers. PhD thesis, ETH, Zürich.

MAEDER, T., ADAMS, N. A. & KLEISER, L. 2001 Direct simulation of turbulent supersonic boundary layers by an extended temporal approach. *J. Fluid Mech.* **429**, 187–216.

MARTÍN, M. P. 2000 Shock-capturing in LES of high-speed flows. *Tech Rep.* Center for Turbulence Research, Stanford University.

MARTÍN, M. P. 2003 Exploratory studies of turbulence/chemistry interaction in hypersonic flows. *AIAA Paper* 2003-4055.

MARTÍN, M. P. 2007 Direct numerical simulation of hypersonic turbulent boundary layers. Part 1. initialization and comparison with experiments. *J. Fluid Mech.* **570**, 347–364.

MARTÍN, M. P. & CANDLER, G. V. 1998 Effect of chemical reactions on decaying isotropic turbulence. *Phys. Fluids* **10**, 1715–1724.

MARTÍN, M. P. & CANDLER, G. V. 1999 Subgrid-scale model for the temperature fluctuations in reacting hypersonic turbulent flows. *Phys. Fluids* **11**.

MARTÍN, M. P. & CANDLER, G. V. 2001 Temperature fluctuation scaling in reacting turbulent boundary layers. *AIAA Paper* 2001-2717.

MARTÍN, M. P., TAYLOR, E. M., WU, M. & WEIRS, V. G. 2006 A bandwidth-optimized WENO scheme for the effective direct numerical simulation of compressible turbulence. *J. Comput. Phys.* **220**, 270–289.

MORKOVIN, M. V. 1962 Effects of compressibility on turbulent flows. In *Mécanique de la Turbulence*, *Colloques Internationaux du Centre National de la Recherche Scientifique*, 108. pp. 367–380. Editions du CNRS.

O'FARRELL, C. & MARTÍN, M. P. 2009 Chasing eddies and their wall signature in DNS data of turbulent boundary layers. *J. Turbul.* **10**, no. 15.

PARK, C. 1990 *Nonequilibrium Hypersonic Aerothermodynamics*, 1st edn. John Wiley & Sons.

PIROZZOLI, S., GRASSO, F. & GATSKI, T. B. 2004 Direct numerical simulation and analysis of a spatially evolving supersonic turbulent boundary layer at $M = 2.25$. *Phys. Fluids* **16** (3), 530–545.

RINGUETTE, M. J., WU, M. & MARTIN, M. P. 2008 Coherent structures in direct numerical simulation of turbulent boundary layers at Mach 3. *J. Fluid Mech.* **594**, 59–69.

ROY, C. J. & BLOTTNER, F. G. 2006 Review and assessment of turbulence models for hypersonic flows. *Prog. Aerosp.* **42**, 469–530.

RUBESIN, M. W. 1990 Extra compressibility terms for Favre-averaged two-equation models of inhomogeneous turbulent flows. *Tech Rep.* 177556. NASA Contractor Rep.

SMITS, A. J. & DUSSAUGE, J. P. 2006 *Turbulent Shear Layers in Supersonic Flow*, 2nd edn. American Institute of Physics.

SPALART, P. R. 1988 Direct simulation of a turbulent boundary layer up to Re_θ equals 1410. *J. Fluid Mech.* **187**, 61–98.

TAYLOR, E. M. & MARTÍN, M. P. 2007 Stencil adaptation properties of a WENO scheme in direct numerical simulation of compressible turbulence. *J. Sci. Comput.* **30** (3), 533–554.

VREMAN, A. W., SANDHAM, N. D. & LUO, K. H. 1996 Compressible mixing layer growth rate and turbulence characteristics. *J. Fluid Mech.* **320**, 235–258.

WALZ, A. 1969 *Boundary Layers of Flow and Temperature*. MIT.

WILCOX, D. C. 2006 *Turbulence Modeling for CFD*, 3rd edn. DCW Industries.

WILLIAMSON, J. H. 1980 Low-storage Runge–Kutta schemes. *J. Comput. Phys.* **35** (1), 48–56.

WRIGHT, M. J., WHITE, T. & MANGINI, N. 2009 Data Parallel Line Relaxation (DPLR) code User Manual; Acadia – Version 4.01.1. *NASA TM* 2009-215388.

XU, S. & MARTÍN, M. P. 2004 Assessment of inflow boundary conditions for compressible turbulent boundary layers. *Phys. Fluids* **16** (7), 2623–2639.

YOS, J. M. 1963 Transport properties of nitrogen, hydrogen, oxygen, and air to 30,000 K. *Avco. Corp. TR AD-TM-63-7*.